

# A Unified Framework for Probabilistic Dynamic-, Trajectory- and Vision-based Virtual Fixtures

Maximilian Mühlbauer<sup>1,2</sup>, Bernhard Weber<sup>2</sup>, Sylvain Calinon<sup>3,4</sup>, Freck Stulp<sup>2</sup>, Alin Albu-Schäffer<sup>2,1</sup>, João Silvério<sup>2</sup>

**Abstract**—Probabilistic Virtual Fixtures (VFs) enable the adaptive selection of the most suitable haptic feedback for each phase of a task, based on learned or perceived uncertainty. While keeping the human in the loop remains essential, for instance, to ensure high precision, partial automation of certain task phases is critical for productivity. We present a unified framework for probabilistic VFs that seamlessly switches between manual fixtures, semi-automated fixtures (with the human handling precise tasks), and full autonomy. We introduce a novel probabilistic Dynamical System-based VF for coarse guidance, enabling the robot to autonomously complete certain task phases while keeping the human operator in the loop. For tasks requiring precise guidance, we extend probabilistic position-based trajectory fixtures with automation allowing for seamless human interaction as well as geometry-awareness and optimal impedance gains. For manual tasks requiring very precise guidance, we also extend visual servoing fixtures with the same geometry-awareness and impedance behavior. We validate our approach experimentally on different robots, showcasing multiple operation modes and the ease of programming fixtures.

**Index Terms**—Human-Centered Automation, Space Robotics and Automation, Learning and Adaptive Systems, Telerobotics and Teleoperation.

## I. INTRODUCTION

**V**IRTUAL Fixtures (VFs) [1], [2] guide humans through tasks by providing haptic feedback. They have been applied to diverse areas such as medical robotics [3], manufacturing on Earth [4] and in space [5]–[8] as well as in underwater manipulation [9]. Depending on the task phase, fixtures can be based on different perceptual input, e.g., on robot proprioception or visual measurements [7], [8]. One main limitation of state-of-the-art VFs is, however, that tasks cannot be accomplished without a human in the loop, raising the need for fixtures that can progress autonomously by outputting actions, e.g. velocities, while still keeping the human in full control. Another limitation is that, when having a set of complementary fixtures with different input modalities, output types and models, as summarized in Table I, a principled arbitration between them is required, which is currently not available. Our main contribution is a framework for the fusion of probabilistic fixtures, ensuring both an optimal guidance for the human and automated operation when needed. A novel set of VFs, providing different types of assistance depending

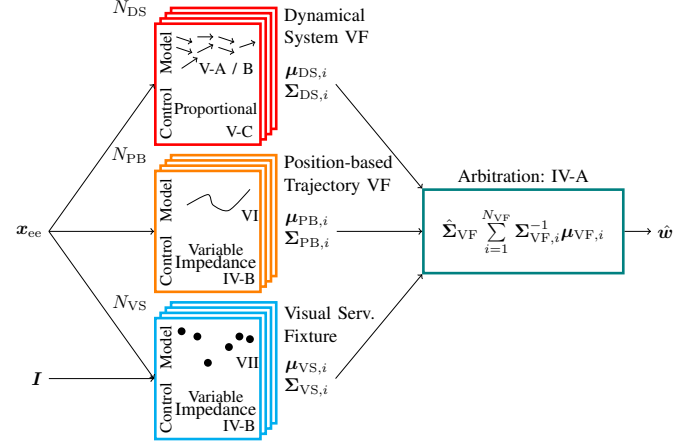


Fig. 1: Overview of our unified framework. We propose a new type of learned, Dynamical Systems based Virtual Fixtures to assist an operator with **coarse guidance** in progressing along the task while staying near the training data. For **precise guidance**, position-based trajectory fixtures support the human operator while geometric visual servoing fixtures provide **very precise guidance**. Core of our framework is a novel variable impedance control scheme as well as an optimal arbitration of all probabilistic fixture wrenches.

on required guidance precision (Table I), forms the backbone of our framework. All our VFs output a probabilistic wrench with covariance in pose space. We formulate the fusion of different VFs in a principled way using an arbitration scheme (Section IV), thus solving the problem of selecting and switching between VFs in a flexible and adaptive manner based on learned and/or perceived uncertainties. Figure 1 provides an overview of our unified framework.

To create automated VFs, we propose a novel probabilistic VF for **coarse guidance** based on learned *Dynamical Systems* (DSs) [10], [11] which have been studied extensively in robotics [12]–[20] and are a promising approach to model a wide range of autonomously executed tasks. Commonly, they are equipped with a single attractor and the method ensures that the system converges to that point. Using probabilistic methods providing epistemic uncertainty we model DSs that do not necessarily converge to a single attractor but may also contain recurring motions and can be composed of multiple demonstrated dynamics in different areas of the robot’s workspace while supporting user interaction (Section V).

While DS-based fixtures offer a very flexible automated assistance, probabilistic *position-based trajectory fixtures* are better suited for **precise guidance** when a demonstrated path has to be followed. Although such fixtures are abundant in the literature [8], [21], in scenarios of potential data scarcity,

<sup>1</sup> School of Computation, Information and Technology, Sensor Based Robotic Systems and Intelligent Assistance Systems, Technical University of Munich, Friedrich-Ludwig-Bauer-Str. 3, Garching, Germany.

<sup>2</sup> German Aerospace Center (DLR), Robotics and Mechatronics Center (RMC), Münchener Str. 20, 82234 Weßling, Germany.

<sup>3</sup> Idiap Research Institute, Martigny, Switzerland.

<sup>4</sup> École Polytechnique Fédérale de Lausanne (EPFL), Switzerland.

TABLE I: TYPES OF FIXTURES CONSIDERED IN OUR FRAMEWORK.

Fixture	Input	Output	Accuracy	Workspace
<i>Dynamical System</i> (V)	Pose	Velocity	Coarse	Everywhere
<i>Position-based Trajectory</i> (VI)	Pose	Pose	Precise	Near trajectory
<i>Visual servoing</i> (VII)	Image	Pose	Very precise	Near target

learning efficiency becomes crucial. To facilitate data efficient learning when object and task geometries are known, we propose an extension of a state-of-the-art formulation [22] to take different geometries into account. Furthermore, extracting the preferred direction from demonstration data, we automate the execution of such fixtures by extending them with a novel control scheme inspired by the DS based VF (Section VI).

For **very precise guidance**, particularly near relevant objects in the robot workspace, we leverage probabilistic visual measurements. The *visual servoing fixture* formulation [8] arbitrates between multiple possible targets. We extend this formulation to cylindrical and spherical manifolds, taking special arrangements of those targets into account (Section VII).

Our proposed probabilistic VF framework reproduces the whole range of automation levels. In *manual* mode, a user is guided by non-progressing VFs in teleoperation or hand-guided mode. *Semi-automated* VFs automate certain tasks while others are still in the responsibility of a human operator. Finally, *fully automated* VFs act autonomously while a human can still intervene. The key contributions of our work are:

- 1) An extended arbitration scheme taking different types of VFs (Table I) and different underlying geometries into account (Section IV-A);
- 2) A novel variable stiffness formulation allowing to model couplings between positional and orientational degrees of freedom (DoFs) (Section IV-B);
- 3) A novel dynamical system based VF (Section V);
- 4) An extension of position-based fixtures to different manifolds as well as their automation (Section VI);
- 5) An extension of visual servoing fixtures to different manifolds (Section VII).

For evaluating our framework, we have implemented it on different robotic systems under different automation levels. After experimentally validating the individual fixtures (Sections VIII-A to VIII-D), we evaluate the combination of fixtures both in a fully automated scenario on a space-ready robot (Section VIII-E) as well as in semi-automated scenarios with human interaction (Sections VIII-F and VIII-G). We provide background on Riemannian manifolds, probabilistic learning from demonstration and impedance control in Section III. Key notations used throughout the work are listed in Table III.

## II. RELATED WORK

Our approach builds on a range of techniques from robot learning and control which we review in this section. The proposed DS-based VF formulation (Section V) builds on the learning of DS body of work [10], [11], [15], [18] as well as on methods for interaction with them, explored in Sections II-A and II-B. For position-based trajectory fixtures (Section VI), automation approaches (Section II-C) and adaptive stiffness scaling (Section II-D) are explored. Finally, we review techniques for the adaptive arbitration of VFs in Section II-E.

### A. Dynamical Systems

Dynamical Systems (DSs) model actions as a function of the system state. As such, they can for example encode velocity policies  $\dot{x} = f(x)$ . Dynamic Movement Primitives (DMPs) [10], [11] model such systems with a single attractor by combining a stable attractor dynamic with forcing terms. Those forcing terms deform the attractor field to e.g. follow complex trajectories. A DMP can be learned by optimizing the parameters of its forcing terms to follow a set of demonstrations as closely as possible. For an overview of popular DMP-based approaches, the reader is referred to [12].

Stable Estimators of Dynamical Systems (SEDS) [15] learns a Gaussian Mixture Model (GMM) and ensures stability of the resulting DS towards an attractor point. For the case of multiple attractors, [16] proposes a clustering method. For complex DSs, [17] proposes to learn the non-linearity of the DS, allowing for an easy adaptation of the learned dynamics with the use case of obstacle avoidance. Learning implicit manifolds promises to better model complex DSs [14]. Neural networks allow for even more powerful estimations of DSs. In [18], global stability of the learned system is ensured through a special network architecture. Other approaches [19], [20] design a special loss function to shape the learned system. At the cost of a loss of a global stability proof, the more powerful expressivity of deep neural networks can be leveraged. Closest to our approach are [23]–[25] which also utilize a stabilizing policy together with the learned nonparametric velocity field. They however integrate the velocity field to positions, leaving user interaction for future work, which our method allows for.

While ensuring convergence to an attractor point, many of the proposed methods exhibit motions which were not demonstrated when far away from demonstrated data and therefore might surprise the operator. Furthermore, it is not possible to fuse multiple of such motion policies in one unified framework. We here propose a non-parametric approach based on Kernelized Movement Primitives (KMPs) leveraging the fusion of different policies (Section V). This allows us to have multiple DSs active in the workspace in parallel that can e.g. each handle a specific portion of a task. Our formulation without fixed attractor points also allows to model periodic motions, e.g. limit cycles. A probabilistic stabilizing policy ensures that the robot always stays close to demonstrated data by computing a velocity towards the closest known dynamic. By using appropriate Riemannian distance metrics in the kernel function, we can account for the full pose as state input.

### B. User Interaction with Dynamical Systems

Conventionally, DSs are used to program autonomous robot motions. Interactions from a human are treated as perturbations and therefore cancelled. In contrast, [26] design a DMP for human interaction. The DMP evolution is synchronized with the human movement and a penetrable VF provides force feedback when the user would deviate from the programmed trajectory. Stiffness scaling is used to allow for user corrections. In [27], a similarly time-synchronized DMP is designed allowing for a shared control scheme where the autonomous agent controls repetitive DoFs while the human operator is responsible for

the required accuracy in the more variable DoFs. Chen et al. [28] sample attractor points from a DS and employ variable stiffness with impedance control which they also combine with a human operator [29].

Closest to our approach is [30] who hand-program a DS for user interaction. An impedance controller is used for torque control of the robot allowing for human interactions. For force-based tasks, a force overlay is added when the robot is in surface contact. The stabilizing properties of the DS are used to bring the robot back to the surface in case of perturbations.

In general, using learned DSs as haptic aids for human operators has received little attention so far. We aim to fill this gap by employing a damping controller (Section V-C) enabling the guidance of a human operator through a state-based DS. The system state evolves both through the actions of the DS as well as through user input. The probabilistic formulation achieves an optimal fusion of different policies as well as between different VFs.

### C. Position-based Trajectory VF Automation

Position-based VFs, which take the robot pose as input and output a desired pose (Table I), have been applied to many teleoperation tasks, e.g., in medical [3], [31] and industrial robotics [32]. They have also been used together with vision [33]. Closest to our work are the probabilistic trajectory fixtures [21], [34]. An overview of different types of fixtures can be found in [2], [35]. Traditionally, VFs constrain the user by keeping them outside of forbidden regions or guiding them along a path without directional guidance [2].

For our framework, an automated version of such fixtures is required. To this end, [36] propose to use the path direction to guide the user along a path. In [3], a cylindrical VF is used to move along a path. For full automation, radius and length of the cylinder are set to 0 which makes the user follow a given trajectory. Automation is achieved by introducing a point mass which is accelerated by a user-defined force - this force is being counteracted by a virtual damping as well as a damping potentially introduced by the user, therefore limiting the maximum velocity. Transitions between different levels of autonomy are possible by enlarging or shrinking the guiding cylinder. None of these approaches however implements more than one concurrently active fixture. Furthermore, no fusion with other types of fixtures is possible with those works. Through a probabilistic fusion, our approach allows us to both model multiple concurrently active trajectory fixtures as well as to fuse the automated fixture with other fixtures.

### D. Virtual Fixtures with Variable Stiffness

Impedance control [37] allows for compliant interaction with the environment and is therefore crucial for safe manipulation as well as robot-human interaction. A key element of this approach is the choice of stiffness matrix, as this matrix determines the relationship between position offset and exerted forces. This key property can be changed according to the task needs using variable stiffness formulations.

To this end, [38] suggest to learn the coupling stiffness for teleoperation. Learned from task properties, the coupling

between input device and remote robot is realized with a low stiffness for safe interactions or with high stiffness to achieve a high tracking accuracy. Other approaches [28], [29] learn a DS with variable stiffness along an orthogonal to the motion direction and furthermore demonstrate it in a shared control application. The approach is also extended to incorporate a learned stiffness for rotational DoFs [39].

Closer to our requirements is [40] where based on the uncertainty of a perception algorithm, the stiffness of the robot controller is adapted through a scaling factor. Covariance matrices can however model complex relationships between the individual DoFs which cannot be represented by a scalar factor. In [41], a block diagonal matrix with submatrices for position and orientation stiffness based on the covariance matrix of a learned trajectory is used. While this choice of stiffness matrix can model a wide range of stiffness behaviors, couplings between positional and orientational DoFs which e.g. full covariance matrices can represent are neglected.

As our experiments underline (Section VIII-A), covariance matrices with couplings between position and orientation are important for variable stiffness control. Note that simply using a scaled version of the precision matrix  $P = \Sigma^{-1}$  is not possible as this might lead to too high stiffness values that might render a physical system unstable. We therefore build upon the findings of [42], [43] who decompose a stiffness matrix into eigenscrews. This can be performed similarly using precision matrices to design a desired stiffness matrix with such couplings while respecting stiffness limits (Section IV-B).

### E. Virtual Fixture Arbitration

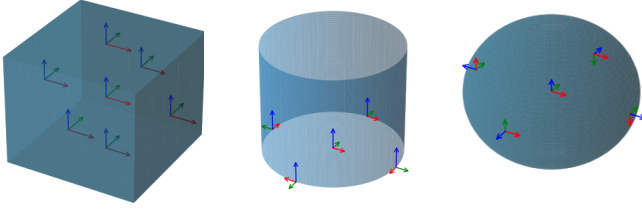
As shown previously [8], a function to arbitrate between different VFs is required, which extends the concept of *arbitration* between human operator and system (see [44] for a survey). To this end, special controllers to stabilize hard switches [45] or hand-tuned weights [7], [46] can be used. One major limitation of these works is that the arbitration function or stabilizing controller does not make use of information from the fixtures but instead needs to be handcrafted.

This limitation can be resolved using probabilistic formulations [21]. Further extensions allow for an individual weighting along all DoFs instead of a single scalar weight value. This can also be used to arbitrate between system and human operator [34], [38]. In a previous work [8] a Gaussian product has been used to perform DoF-specific arbitration. We build on this foundation to include all fixtures highlighted in Table I in a unified framework, showing how DS based VFs (Section V) and VFs on different geometries can be fused (Section IV-A).

## III. BACKGROUND

### A. Riemannian Manifolds and Probabilities

The geometry of a task can be modeled using Riemannian manifolds – this is already required for orientations which are non-Euclidean. Following the notation and intuition of [22] on when to use which manifold, we consider the manifolds  $\mathcal{M}$  shown in Fig. 2 to express a full pose  $x$ :



(a)  $\mathcal{M}_1: \mathbb{R}^3 \times \mathcal{S}^3$ . (b)  $\mathcal{M}_2: \mathcal{S}^1 \times \mathbb{R}^2 \times \mathcal{S}^3$ . (c)  $\mathcal{M}_3: \mathcal{S}^2 \times \mathbb{R}^1 \times \mathcal{S}^3$ .

Fig. 2: Manifolds used in this work inspired by and using the notation of [22]. Depending on the task, properties can be expressed more efficiently in cylindrical ( $\mathcal{M}_2$ ) or spherical ( $\mathcal{M}_3$ ) compared to Cartesian ( $\mathcal{M}_1$ ) coordinates. The coordinate systems in each image depict the orientation basis, i.e. the unit quaternion  $(0, 0, 0, 1)^\top$  for different positions on the manifold.

- 1)  $\mathcal{M}_1$  with  $\mathbf{x} \in \mathbb{R}^3 \times \mathcal{S}^3$ : We use this manifold to represent Cartesian poses as product of the position expressed in 3-dimensional Euclidean space and a unit quaternion<sup>1</sup>.
- 2)  $\mathcal{M}_2$  with  $\mathbf{x} \in \mathcal{S}^1 \times \mathbb{R}^2 \times \mathcal{S}^3$ : This manifold represents cylindrical poses as product of the angle  $\phi$  from the  $x$ -axis, the radius  $r$  measured as distance from the origin in the  $xy$  plane and the  $z$  coordinate and a unit quaternion. The base of the orientation is adjusted such that its  $y$  axis is always pointing in direction of increasing radius.
- 3)  $\mathcal{M}_3$  with  $\mathbf{x} \in \mathcal{S}^2 \times \mathbb{R}^1 \times \mathcal{S}^3$ : We use this manifold to represent spherical poses as product of the angles from the  $x$  and  $z$  axis (often denoted as *azimuthal* angle  $\phi$  and *polar* angle  $\theta$ ), the radius  $r$  and a unit quaternion. The base of the orientation is adjusted such that the  $z$  axis is always pointing in direction of increasing radius.

The manifold logarithm  $\text{Log}_{\mathbf{x}_1}^{\mathcal{M}} \mathbf{x}_2$  on  $\mathcal{M}$  calculates the tangent vector  $\mathbf{u}_{12} \in \mathcal{T}_{\mathbf{x}_1} \mathcal{M}$  from  $\mathbf{x}_1$  in the direction of  $\mathbf{x}_2$ , its magnitude is equal to the geodesic distance between the points. Its inverse, the manifold exponential  $\text{Exp}_{\mathbf{x}_1}^{\mathcal{M}} \mathbf{u}_{12}$ , allows to recover  $\mathbf{x}_2$  on the manifold. Parallel transport is required to move vectors between different tangent spaces centered at  $\mathbf{x}_i$ . The reader is referred to [47], [48] for a more exhaustive treatment of these Riemannian operations. Between tangent spaces of different manifolds, manifold-specific Jacobians  $\mathbf{J}_{\mathcal{M}}$  (see Section H) transform vectors *contravariantly* [49].

With the logarithm map and the Gaussian distribution proposed by [47], [48], we compute the probability of  $\mathbf{x}$  to

$$\mathcal{N}(\mathbf{x} | \boldsymbol{\mu}, \boldsymbol{\Sigma}) = \frac{1}{\sqrt{(2\pi)^d |\boldsymbol{\Sigma}|}} e^{-\frac{1}{2} \text{Log}_{\boldsymbol{\mu}}^{\mathcal{M}}(\mathbf{x})^\top \boldsymbol{\Sigma}^{-1} \text{Log}_{\boldsymbol{\mu}}^{\mathcal{M}}(\mathbf{x})}, \quad (1)$$

parameterized by mean  $\boldsymbol{\mu} \in \mathcal{M}$  and covariance  $\boldsymbol{\Sigma} \in \mathcal{T}_{\boldsymbol{\mu}} \mathcal{M}$ .

Finally, a weighted distance measure between  $\mathbf{x}_1$  and  $\mathbf{x}_2$  is often required. For this, we define the on-manifold distance

$$\begin{aligned} d_{\mathbf{A}}^{\mathcal{M}}(\mathbf{x}_1, \mathbf{x}_2) &= \left\| \text{Log}_{\mathbf{x}_1}^{\mathcal{M}} \mathbf{x}_2 \right\|_{\mathbf{A}}^2 \\ &= \text{Log}_{\mathbf{x}_1}^{\mathcal{M}}(\mathbf{x}_2)^\top \mathbf{A} \text{Log}_{\mathbf{x}_1}^{\mathcal{M}}(\mathbf{x}_2). \end{aligned} \quad (2)$$

with a weighting matrix  $\mathbf{A}$  expressed in tangent space  $\mathcal{T}_{\mathbf{x}_1} \mathcal{M}$ . Note that e.g. in the case of  $\mathcal{S}^2$ ,  $\text{Log}_{\mathbf{x}_1}^{\mathcal{S}^2} \mathbf{x}_2 \neq -\text{Log}_{\mathbf{x}_2}^{\mathcal{S}^2} \mathbf{x}_1$  as would hold for the other manifolds used in this work. For a change of basis,  $\mathbf{A}$  therefore would have to be rotated.

<sup>1</sup>To avoid issues with  $\mathcal{S}^3$  double-covering  $SO(3)$ , we wrap the logarithm at a full rotation, ensuring that  $\text{Log}_{\mathbf{q}}(-\mathbf{q}) = \mathbf{0}$ .

## B. Impedance-controlled Virtual Fixtures

Our Virtual Fixtures framework (Section IV) outputs a Cartesian wrench  $\mathbf{w}_{\text{VF}}$  which is applied to the end effector. Assuming a gravity-compensated, torque-controlled manipulator, the corresponding desired joint torques evaluate to

$$\boldsymbol{\tau} = \mathbf{J}^\top \mathbf{w}_{\text{VF}}. \quad (3)$$

Note that  $\mathbf{w}_{\text{VF}}$  is a covector in cotangent space  $\mathcal{T}_{\mathbf{x}_{\text{ee}}}^* \mathcal{M}$  ( $\eta: \mathcal{T}_{\mathbf{x}_{\text{ee}}} \mathcal{M} \rightarrow \mathbb{R}$ ) requiring the covariant transformation with  $\mathbf{J}_{\mathcal{M}}^\top$  [49] following from the conservation of power  $\boldsymbol{\tau}^\top \dot{\mathbf{q}} = \mathbf{w}^\top \dot{\mathbf{x}}$ . We assume that  $\mathbf{w}_{\text{VF}}$  is a combination of  $N_{\text{VF}} = N_{\text{DS}} + N_{\text{PB}} + N_{\text{VS}}$  individual wrenches associated with different VFs. For position-based VFs (Section VI), this wrench is computed as

$$\mathbf{w}_{\text{VF},i} = \mathbf{K}_{\text{VF},i} \text{Log}_{\mathbf{x}_{\text{ee}}}^{\mathcal{M}}(\mathbf{x}_{\text{VF},i}) + \mathbf{D}_{\text{VF},i} \frac{d}{dt} \text{Log}_{\mathbf{x}_{\text{ee}}}^{\mathcal{M}}(\mathbf{x}_{\text{VF},i}), \quad (4)$$

where  $\mathbf{x}_{\text{ee}} \in \mathcal{M}$  is the end effector pose.  $\mathbf{K}_{\text{VF},i}$ ,  $\mathbf{D}_{\text{VF},i}$  and  $\mathbf{x}_{\text{VF},i}$  are the stiffness, damping and attractor of the fixture.  $\text{Log}_{\mathbf{x}_{\text{ee}}}^{\mathcal{M}}(\mathbf{x}_{\text{VF}})$  denotes the manifold logarithm [47] of  $\mathbf{x}_{\text{VF}}$  at  $\mathbf{x}_{\text{ee}}$ , which is the on-manifold equivalent to the Euclidean  $\mathbf{x}_{\text{VF},i} - \mathbf{x}_{\text{ee}}$ , taking orientation and different manifolds  $\mathcal{M}$  into account.  $\frac{d}{dt} \text{Log}_{\mathbf{x}_{\text{ee}}}^{\mathcal{M}}(\mathbf{x}_{\text{VF}})$  is the corresponding time derivative. We compute a single Cartesian wrench  $\mathbf{w}_{\text{VF}}$  for (3) from impedance- and velocity-controlled fixtures  $\mathbf{w}_{\text{VF},i}$  on different manifolds through a probabilistic fusion (Section IV-A).

## C. Probabilistic Learning from Demonstration

Different probabilistic models encoding assistive behaviors can be learned from demonstration data using Gaussian distributions. We are specifically interested to model both the *aleatoric* uncertainty which is inherent to the data, i.e. the variability in demonstrations, as well as the *epistemic* uncertainty, which is the uncertainty caused by a lack of data. We argue that fixture activation should be inversely proportional to uncertainty – both epistemic and aleatoric – such that strong guidance corresponds to low uncertainty levels.

GMMs [48], [50] encode the joint distribution between input  $\mathbf{x}$  and output  $\mathbf{y}$  with  $M$  Gaussians, i.e.

$$\begin{bmatrix} \mathbf{x} \\ \mathbf{y} \end{bmatrix} \sim \sum_{m=1}^M \pi_m \mathcal{N} \left( \begin{bmatrix} \mathbf{x} \\ \mathbf{y} \end{bmatrix} \middle| \boldsymbol{\mu}_m, \boldsymbol{\Sigma}_m \right). \quad (5)$$

The conditional distribution of  $\mathbf{y}$  given  $\mathbf{x}$  can be computed as

$$p(\mathbf{y} | \mathbf{x}) = \sum_{m=1}^M \pi_m(\mathbf{x}) \mathcal{N}(\mathbf{y} | \boldsymbol{\mu}_{m|\mathbf{x}}, \boldsymbol{\Sigma}_{m|\mathbf{x}}) \quad (6)$$

using Gaussian Mixture Regression (GMR). Note that this is a Mixture of Experts (MoE) [51] model, computing a multi-modal weighted sum of different experts represented by Gaussian distributions in an “or” operation. Subsequently, a unimodal approximation can be computed as [50]

$$p(\mathbf{y} | \mathbf{x}) = \mathcal{N}(\mathbf{y} | \boldsymbol{\mu}_{\text{GMR}}, \boldsymbol{\Sigma}_{\text{GMR}}) \quad (7)$$

which is used in (Section VI) to derive position-based trajectory fixtures. For geometry-awareness we use the on-manifold Gaussian operations from [47]. The GMM’s covariance reflects *aleatoric* uncertainty which is used to scale stiffness (Section IV-B), preserving the demonstrated variability.

Kernel-based methods such as Gaussian Processes (GPs) [52] and KMPs [53] output *epistemic* uncertainty which increases with the distance between training data and new inputs. Notably, the latter is capable of capturing both *aleatoric* and *epistemic* uncertainties. This is used in the DS-based VF (Section V) to find validity regions for learned dynamics. In KMPs, the posterior mean and covariance of a function  $y = f(x)$  are computed. For a test point  $\mathbf{x}^*$ , we obtain

$$\boldsymbol{\mu}^* = \mathbf{K}(\mathbf{x}^*, \mathbf{x}) (\mathbf{K}(\mathbf{x}, \mathbf{x}) + \lambda \boldsymbol{\Sigma})^{-1} \boldsymbol{\mu} \quad (8)$$

$$\boldsymbol{\Sigma}^* = \alpha (\mathbf{K}(\mathbf{x}^*, \mathbf{x}^*) - \mathbf{K}(\mathbf{x}^*, \mathbf{x}) (\mathbf{K}(\mathbf{x}, \mathbf{x}) + \lambda_c \boldsymbol{\Sigma})^{-1} \mathbf{K}(\mathbf{x}, \mathbf{x}^*)). \quad (9)$$

$\mathbf{k}(\mathbf{x}_i, \mathbf{x}_j) = k(\mathbf{x}_i, \mathbf{x}_j) \mathbf{I}$ , where  $k(\mathbf{x}_i, \mathbf{x}_j)$  is a kernel function<sup>2</sup>,  $\boldsymbol{\mu} = [\boldsymbol{\mu}_1^\top, \dots, \boldsymbol{\mu}_N^\top]^\top$  and  $\boldsymbol{\Sigma} = \text{blockdiag}(\boldsymbol{\Sigma}_1, \dots, \boldsymbol{\Sigma}_N)$  are set from a probabilistic reference.  $\lambda$ ,  $\lambda_c$  and  $\alpha$  are regularization and scaling hyperparameters. Please see [53] for a detailed derivation. Note the connection to classical GPs [52], where we have  $\lambda_c = \lambda$  and  $\boldsymbol{\Sigma} = \mathbf{I}$  (*homoscedasticity*),  $\alpha = 1$  and  $\boldsymbol{\mu}$  are directly the observations  $\mathbf{y}$ .

Treating GMM and KMP predictions as experts, we fuse outputs using a Product of Experts (PoE) [55] in an “and” operation where each constraint is satisfied approximately, allowing for an arbitration between different types and representations of VFs (Section IV-A).

#### IV. VIRTUAL FIXTURE FRAMEWORK

We assume that depending on the specific task at hand, Virtual Fixtures (VFs) with different properties are required to optimally guide an operator or to automate the task. Table I summarizes properties of the individual VFs we consider. Common for all our fixtures is that they output probabilistic wrenches with on-manifold, multivariate Gaussian uncertainties

$$p(\mathbf{w}_{\text{VF},i}) = \mathcal{N}(\boldsymbol{\mu}_{\text{VF},i}, \boldsymbol{\Sigma}_{\text{VF},i}) \quad (10)$$

where  $\boldsymbol{\mu}_{\text{VF},i}$  is the mean of the wrench calculated by each fixture on its specific manifold (Fig. 2), under the assumption that  $\mathbf{w}_{\text{VF},i}$  is Gaussian-distributed. This allows for a natural arbitration between fixtures using the covariance  $\boldsymbol{\Sigma}_{\text{VF},i}$ , taking also DoF-specific uncertainty and correlations into account. The arbitration is detailed in Section IV-A. For impedance-controlled VFs, the covariance can also be used to modulate the stiffness. Our novel approach to achieve fully populated stiffness matrices is detailed in Section IV-B.

Figure 3 shows the different coordinate systems used by our method. An easy transfer between different object placements is possible through the task coordinate system. Coordinates for individual fixtures placed relative to this coordinate system allow us to exploit the properties of different geometries.

##### A. Virtual Fixture Arbitration

Previous works [8] use a PoE [55] to perform the arbitration of different fixture wrenches expressed in the same coordinate

system. Extending this, we furthermore consider the fixture-specific manifolds depicted in Fig. 2. Each fixture outputs a mean wrench  $\boldsymbol{\mu}_{\text{VF},i,\mathcal{M}}$  in the cotangent space  $\mathcal{T}_{\mathbf{x}_{\text{ee}}}^* \mathcal{M}$  of a specific manifold  $\mathcal{M}$  through (4). This prohibits a direct fusion of the fixture wrenches as the entries in the wrench covector correspond to different DoFs. In order to stay robot agnostic, we propose to transform covariances and mean wrenches into the (co)tangent space  $\mathcal{T}_{\mathbf{x}_{\text{ee}}}^{(*)} \mathcal{M}_1$  using

$$\boldsymbol{\mu}_{\text{VF},i,\mathcal{M}_1} = \mathbf{J}_{i,\mathcal{M}}^\top \boldsymbol{\mu}_{\text{VF},i,\mathcal{M}} \quad (11)$$

$$\boldsymbol{\Sigma}_{\text{VF},i,\mathcal{M}_1} = \mathbf{J}_{i,\mathcal{M}}^{-1} \boldsymbol{\Sigma}_{\text{VF},i,\mathcal{M}} \mathbf{J}_{i,\mathcal{M}}^{-\top} \quad (12)$$

with the manifold Jacobian  $\mathbf{J}_{i,\mathcal{M}} = \frac{\partial \mathbf{x}_{\text{ee},i,\mathcal{M}}}{\partial \mathbf{x}_{\text{ee},\mathcal{M}_1}}$  [56] given in Section I. This corresponds to the transformation of the covector  $\boldsymbol{\mu}_{\text{VF},i}$  from  $\mathcal{T}_{\mathbf{x}_{\text{ee}}}^* \mathcal{M}$  into  $\mathcal{T}_{\mathbf{x}_{\text{ee}}}^* \mathcal{M}_1$  as well as of the twice contravariant tensor  $\boldsymbol{\Sigma}_{\text{VF}}$  from  $\mathcal{T}_{\mathbf{x}_{\text{ee}}} \mathcal{M}$  into  $\mathcal{T}_{\mathbf{x}_{\text{ee}}} \mathcal{M}_1$ .

The wrench  $\boldsymbol{\mu}_{\text{VF},i,\mathcal{M}_1}$  in cotangent space  $\mathcal{T}_{\mathbf{x}_{\text{ee}}}^* \mathcal{M}_1$  expresses the forces of the wrench in the `FIXTURE` coordinate system while the torques are expressed in `TOOL` coordinates (Fig. 3). Compared to that, the SE(3) wrench required by (3) expects also the forces in `TOOL` coordinates which corresponds to a rotation of the position part of the tangent space. The mean wrench  $\boldsymbol{\mu}_{\text{VF},i}$  of each fixture  $i$  to be commanded at the end effector is thus transformed from  $\mathcal{T}_{\mathbf{x}_{\text{ee}}}^* \mathcal{M}_1$  to  $\mathfrak{se}(3)$  using

$$\boldsymbol{\mu}_{\text{VF},i,\text{SE3}} = \begin{bmatrix} \mathbf{R}_{\text{ee}}^\top & \mathbf{0} \\ \mathbf{0} & \mathbf{I} \end{bmatrix} \boldsymbol{\mu}_{\text{VF},i,\mathcal{M}_1}, \quad (13)$$

where  $\mathbf{R}_{\text{ee}}$  is the rotation of  $\mathbf{x}_{\text{ee}}$  in the fixture’s coordinate system. The covariance has to be rotated as well using

$$\boldsymbol{\Sigma}_{\text{VF},i,\text{SE3}} = \begin{bmatrix} \mathbf{R}_{\text{ee}}^\top & \mathbf{0} \\ \mathbf{0} & \mathbf{I} \end{bmatrix} \boldsymbol{\Sigma}_{\text{VF},i,\mathcal{M}_1} \begin{bmatrix} \mathbf{R}_{\text{ee}} & \mathbf{0} \\ \mathbf{0} & \mathbf{I} \end{bmatrix}. \quad (14)$$

$\boldsymbol{\mu}_{\text{VF},i,\text{SE3}}$  and  $\boldsymbol{\Sigma}_{\text{VF},i,\text{SE3}}$  are then used as experts in a PoE (cf. [8]) to calculate the arbitrated  $\hat{\mathbf{w}}$  as result of the optimization

$$\hat{\mathbf{w}} = \arg \min_{\mathbf{w}} \sum_{i=1}^{N_{\text{VF}}} (\mathbf{w} - \boldsymbol{\mu}_{\text{VF},i,\text{SE3}})^\top \boldsymbol{\Sigma}_{\text{VF},i}^{-1} (\mathbf{w} - \boldsymbol{\mu}_{\text{VF},i,\text{SE3}}), \quad (15)$$

solved as product of  $N_{\text{VF}} = N_{\text{DS}} + N_{\text{PB}} + N_{\text{VS}}$  Gaussians

$$\hat{\mathbf{w}} = \hat{\boldsymbol{\Sigma}}_{\text{VF}} \sum_{i=1}^{N_{\text{VF}}} \boldsymbol{\Sigma}_{\text{VF},i}^{-1} \mathbf{w}_{\text{VF},i}, \quad \hat{\boldsymbol{\Sigma}}_{\text{VF}} = \left( \sum_{i=1}^{N_{\text{VF}}} \boldsymbol{\Sigma}_{\text{VF},i}^{-1} \right)^{-1}. \quad (16)$$

The resulting  $\hat{\mathbf{w}}$  with the optimally weighted wrenches of the individual fixtures is then applied to the robot through (3).

##### B. Variable Impedance Control

Modulating the controller stiffness, as a form of authority allocation, allows to assign a higher importance to the fixture in case of low uncertainty and give the operator more freedom otherwise. Using a full covariance matrix, our fixtures can also express DoF specific and coupled uncertainties. To reproduce these properties in the robot’s impedance behavior, we propose a method to match the stiffness characteristics to those of the covariance matrix. Unlike previous works [40], [41], we create a full stiffness matrix with nonzero coupling terms  $\mathbf{K}_{tr}$

$$\mathbf{K} = \begin{bmatrix} \mathbf{K}_t & \mathbf{K}_{tr} \\ \mathbf{K}_{tr}^\top & \mathbf{K}_r \end{bmatrix}. \quad (17)$$

<sup>2</sup>We use (2) with  $\mathbf{A} = \mathbf{I}$  to calculate the on-manifold distance in the kernel. More complex treatments might be required in other use cases [54].

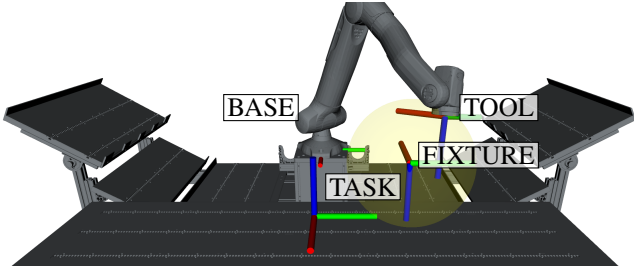


Fig. 3: The [TASK] coordinate system defined with respect to the robot [BASE] allows to account for different object placements in the workspace while the specification of [FIXTURE] coordinate systems relative to the [TASK] coordinate system is crucial for cylindrical and spherical coordinates. Finally, the [TOOL] frame depends on the current end effector pose of the robot.

A first approach could compute  $\mathbf{K}_i = k\Sigma_{VF,i}^{-1}$  using  $k$  to scale the precision matrix. This is however too naïve, as maximum stiffness values in a robotic system are not respected. Furthermore, vastly different scales of stiffness values for translation (e.g.  $2000 \frac{\text{N}}{\text{m}}$ ) and rotation (e.g.  $50 \frac{\text{N}\cdot\text{m}}{\text{rad}}$ ) are neglected.

We therefore propose to decompose the covariance matrix  $P_{VF,i}$  and reassemble it to a stiffness matrix while preserving its properties to the extent possible. Building on the findings of [57], [58] on the decomposition of spatial stiffness matrices, we decompose a rotated precision matrix  $P'_{VF,i}$  into translational ( $P_{t,VF,i}$ ) and rotational ( $P_{r,VF,i}$ ) components

$$P'_{VF,i} = \begin{bmatrix} \mathbf{A} & \mathbf{B} \\ \mathbf{B}^\top & \mathbf{C} \end{bmatrix} = P_{t,VF,i} + P_{r,VF,i} = \begin{bmatrix} \mathbf{A} & \mathbf{B} \\ \mathbf{B}^\top & \mathbf{B}^\top \mathbf{A}^{-1} \mathbf{B} \end{bmatrix} + \begin{bmatrix} \mathbf{0} & \mathbf{0} \\ \mathbf{0} & \mathbf{C} - \mathbf{B}^\top \mathbf{A}^{-1} \mathbf{B} \end{bmatrix}. \quad (18)$$

where  $P_{VF,i}$  is rotated with  $\mathbf{R}_{\text{diag},i}$  to obtain

$$P'_{VF,i} = \begin{bmatrix} \mathbf{R}_{\text{diag},i} & \mathbf{0} \\ \mathbf{0} & \mathbf{R}_{\text{diag},i} \end{bmatrix}^\top P_{VF,i} \begin{bmatrix} \mathbf{R}_{\text{diag},i} & \mathbf{0} \\ \mathbf{0} & \mathbf{R}_{\text{diag},i} \end{bmatrix} \quad (19)$$

and  $\mathbf{R}_{\text{diag},i}$  is chosen s.t.  $\mathbf{A}$  only contains diagonal entries.

$P_{t,VF,i}$  and  $P_{r,VF,i}$  can be further decomposed and after a scaling be realized using three screw springs and three rotational springs, respectively [57]. An eigendecomposition of  $P_{r,VF,i}$  yields the torsional spring axes ( $j = 4, 5, 6$ ) as eigenvectors  $\mathbf{w}_j = (0, 0, 0, w_{rx,j}, w_{ry,j}, w_{rz,j})^\top$  and corresponding eigenvalues  $\lambda_j$ . Those eigenvalues allow to compute a scaling

$$s_j = \begin{cases} 0, & \lambda_j < \lambda_{\text{rot}}^- \\ \frac{\lambda_j - \lambda_{\text{rot}}^-}{\lambda_{\text{rot}}^+ - \lambda_{\text{rot}}^-}, & \lambda_{\text{rot}}^- < \lambda_j < \lambda_{\text{rot}}^+ \\ 1, & \lambda_j \geq \lambda_{\text{rot}}^+ \end{cases}, \quad (20)$$

where  $\lambda_{\text{rot}}^-$  and  $\lambda_{\text{rot}}^+$  are empirically determined hyperparameters for “low” and “high” eigenvalues resulting in full and zero stiffness. The torsional springs are then realized as ( $j = 4, 5, 6$ )

$$\mathbf{K}'_j = k_{\text{nom},j} s_j \mathbf{w}_j \mathbf{w}_j^\top \quad (21)$$

with the nominal stiffnesses  $\mathbf{k}_{\text{nom}} = (k_t, k_t, k_t, k_r, k_r, k_r)^\top$  where  $k_t$  is the translational and  $k_r$  the rotational stiffness. Eigenvalues  $\geq \lambda_{\text{rot}}^+$  result in a nominal stiffness along the corresponding rotational DoF while eigenvalues  $< \lambda_{\text{rot}}^-$  result in zero stiffness with linear scaling in between.

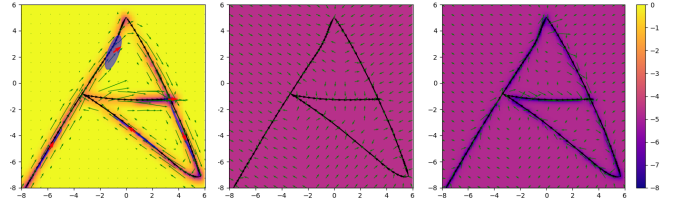


Fig. 4: 2D motion policy using a KMP. Black arrows visualize velocities in the training data [59]. The KMP output is shown on the left (Section V-A), blue ellipsoids and red arrows depict centers, position covariances and velocities of the Gaussians in the reference GMM. The *stabilizing policy* (Section V-B) is shown in the middle, final velocities resulting from the arbitration on the right. The colormap of each plot depicts  $\log(\det(\Sigma))$ .

The screw springs ( $j = 1, 2, 3$ ) are given by wrench axes  $\mathbf{w}_j = (e_j^\top, w_{tx,j}, w_{ty,j}, w_{tz,j})^\top$  with  $[e_1 \ e_2 \ e_3] = \mathbf{I}_3$  and corresponding  $\lambda_j$  from the diagonal entries of  $\mathbf{A}$  in  $P_t$ . The scaling  $s_j$  of (20) is also computed with factors  $\lambda_{\text{trans}}^-$  and  $\lambda_{\text{trans}}^+$ . We limit the rotational stiffness of  $\mathbf{w}_j$  by ensuring

$$s_j \leq \frac{k_r}{k_{\text{nom},j} \sqrt{w_{tx,j}^2 + w_{ty,j}^2 + w_{tz,j}^2}}. \quad (22)$$

While this operation impacts the coupling of translations and rotations in the screw spring, it ensures attainable stiffnesses close to the characteristics of the original precision matrix  $P_{VF,i}$ . The wrench springs are then realized to ( $j = 1, 2, 3$ )

$$\mathbf{K}'_j = k_{\text{nom},j} s_j \mathbf{w}_j \mathbf{w}_j^\top. \quad (23)$$

The resulting stiffness matrix is then calculated from wrench ( $j = 1, 2, 3$ ) and torsional ( $j = 4, 5, 6$ ) springs and rotated

$$\mathbf{K}_i = \begin{bmatrix} \mathbf{R}_{\text{diag},i} & \mathbf{0} \\ \mathbf{0} & \mathbf{R}_{\text{diag},i} \end{bmatrix} \left( \sum_{j=1}^6 \mathbf{K}'_j \right) \begin{bmatrix} \mathbf{R}_{\text{diag},i} & \mathbf{0} \\ \mathbf{0} & \mathbf{R}_{\text{diag},i} \end{bmatrix}^\top \quad (24)$$

$\mathbf{K}_i$  is then used for impedance control (55) of the  $i$ -th fixture.

In Section VIII-A, we show how this approach couples translational and rotational DoFs in the stiffness matrix. Please see Section B for the extension to manifolds  $\mathcal{M}_2$  and  $\mathcal{M}_3$  and Section C for an optimal damping calculation.

## V. PROBABILISTIC DYNAMICAL SYSTEM VIRTUAL FIXTURES

We introduce automated Dynamical System based Virtual Fixtures for **coarse guidance** modeling the relation between assistive velocities  $\dot{\mathbf{x}}_{\text{DS}}$  and robot state  $\mathbf{x}_{\text{ee}}$  probabilistically

$$p(\dot{\mathbf{x}}_{\text{DS}} | \mathbf{x}_{\text{ee}}) = \mathcal{N}(\dot{\mathbf{x}}_{\text{DS}} | \boldsymbol{\mu}_{\text{DS}}, \boldsymbol{\Sigma}_{\text{DS}}), \quad (25)$$

where  $\boldsymbol{\mu}_{\text{DS}}$  denotes the mean of the dynamical system evaluated at  $\mathbf{x}_{\text{ee}}$  and  $\boldsymbol{\Sigma}_{\text{DS}}$  the associated covariance. In contrast to time-driven motions, these models encode state-dependent dynamic behaviors that support user progression along the task, adapting their guidance with varying granularity, such as modulating velocity magnitude based on the task phase or enabling periodic motions. This distinguishes DS-based fixtures from the trajectory-based fixtures (Section VI) which can only encode a trajectory with start and end point. By providing motion information for the whole robot workspace, they are

especially suited to the approaching phase of a manipulation where the robot may start at arbitrary configurations.

We adopt an uncertainty-aware, non-parametric approach that is highly flexible to composition and modulation without requiring parameter re-computation. Based on demonstration data, we use KMPs (Section III-C) to encode a specific task in a region of the workspace which results in  $N_{\text{DS}}$  concurrently active velocity fields on possibly different manifolds. In the following,  $p_n(\dot{\mathbf{x}}_{\text{DS}})$  denotes the  $n$ -th of  $N_{\text{DS}} - 1$  probabilistic DS models learned from demonstrations (see Section V-A), and  $p_{\text{stab}}(\dot{\mathbf{x}}_{\text{DS}})$  a probabilistic policy (see Section V-B) with a constant, pre-defined uncertainty that drives the robot toward the closest known dynamic. A proportional control scheme (Section V-C) enables the use of such learned DS as probabilistic VF. Through our arbitration scheme (Section IV-A), we leverage the epistemic uncertainty encoded by KMPs to automatically prioritize models with low uncertainty. When all models exhibit high uncertainty, the formulation defaults to the stabilizing policy  $p_{\text{stab}}(\dot{\mathbf{x}})$  or to another type of fixture, such as those introduced in Sections VI and VII.

#### A. Non-parametric Learning of Dynamical Systems

We define the  $n$ -th DS as a probabilistic mapping

$$p_n(\dot{\mathbf{x}}_{\text{DS}}|\mathbf{x}_{\text{ee}}) = \mathcal{N}(\dot{\mathbf{x}}_{\text{DS}}|\boldsymbol{\mu}_{\text{DS},n}, \boldsymbol{\Sigma}_{\text{DS},n}) \quad (26)$$

which can be learned from a dataset of demonstrations  $\{\mathbf{x}_j, \dot{\mathbf{x}}_j\}_{j=1}^N$  where e.g. a full pose  $\mathbf{x} \in \mathbb{R}^3 \times \mathcal{S}^3$  ( $\mathcal{M}_1$ ) or only the position part  $\mathbf{x} \in \mathbb{R}^3$  with velocities in the tangent spaces  $\dot{\mathbf{x}} \in \mathcal{T}_{\mathbf{x}}\mathcal{M}$  respectively  $\dot{\mathbf{x}} \in \mathcal{T}_{\mathbf{x}}\mathbb{R}^3 = \mathbb{R}^3$  are used. This dataset is subsampled with equal spacing of the input poses to achieve a trade off between accuracy and computational cost. The demonstrations are then used to learn a KMP (Section III-C). For the use in a DS, we customize the computation of the reference distribution as detailed in Section E.

In our experiments, we use the on-manifold Radial Basis Function (RBF) kernel with the distance function (2)

$$k(\mathbf{x}, \mathbf{x}_{\text{ee}}) = \exp\left(-\frac{d_{\mathbf{I}}^{\mathcal{M}}(\mathbf{x}, \mathbf{x}_{\text{ee}})}{2l^2}\right), \quad (27)$$

where  $l$  denotes the length scale. Similarly to GPs, we assume a zero-mean prior, so predictions from (8) yield  $\dot{\mathbf{x}}_{\text{DS}} = \mathbf{0}$  in regions far from the demonstrations. Moreover, (9) captures aleatoric uncertainty near the data and reflects increasing epistemic uncertainty in regions with limited or no demonstrations. The distance function in (27) naturally extends to the manifold  $\mathcal{M}$  chosen for the task. We treat the output as Euclidean, therefore, only the kernel has to be adapted to the manifold case assuming that the learned velocities are smooth and the length scale parameter of the kernel is small compared to the changes of the velocity.

#### B. Probabilistic Stabilizing Policy

Outside of the task space regions where demonstrations were provided, the robot actions computed from (26) are zero, leaving the robot stationary. A probabilistic *stabilizing policy*<sup>3</sup>

$$p_{\text{stab}}(\dot{\mathbf{x}}_{\text{DS}}|\mathbf{x}_{\text{ee}}) = \mathcal{N}(\dot{\mathbf{x}}_{\text{DS}}|\boldsymbol{\mu}_{\text{stab}}, \boldsymbol{\Sigma}_{\text{stab}}) \quad (28)$$

<sup>3</sup>This policy is not stabilizing in a sense of ensuring convergence but a *soft* stability bringing the robot back to regions of learned DSs.

then brings the robot back into the demonstrated areas. To achieve this, we compute the distance to the reference poses of all  $N_{\text{DS}}$  velocity fields using (2) to  $d_j = d_{\mathbf{I}}^{\mathcal{M}_1}(\mathbf{x}_j, \mathbf{x}_{\text{ee}})$  and obtain the closest pose  $\mathbf{x}_{j^*}$  of a known dynamic with

$$j^* = \underset{j}{\operatorname{argmin}} d_j. \quad (29)$$

The normalized velocity towards this pose using the on-manifold distance (2) and default velocity  $\dot{\mathbf{x}}_{\text{stab}}$  evaluates to

$$\boldsymbol{\mu}_{\text{stab}} = \dot{\mathbf{x}}_{\text{stab}} \frac{\operatorname{Log}_{\mathcal{S}\mathbf{x}_{\text{ee}}}^{\mathcal{M}_1}(\mathbf{x}_{j^*})}{\sqrt{d_{\mathbf{I}}^{\mathcal{M}}(\mathbf{x}_{\text{ee}}, \mathbf{x}_{j^*})}} \quad (30)$$

which is furthermore equipped with a constant covariance

$$\boldsymbol{\Sigma}_{\text{stab}} = \sigma_{\text{stab}} \mathbf{I}_6. \quad (31)$$

The covariance  $\sigma_{\text{stab}}$  of this policy is an important hyperparameter – it has to be chosen such that  $\boldsymbol{\Sigma}_{\text{stab}}$  is bigger than the covariances  $\boldsymbol{\Sigma}_{\text{DS},n}$  of the learned DSs in the areas where demonstrations have been provided. Thanks to KMPs providing epistemic uncertainty, the covariances  $\boldsymbol{\Sigma}_{\text{DS},n}$  increase outside of the demonstrated areas, therefore activating the stabilizing policy which brings the robot back inside the demonstrated areas through the arbitration (16).

Fig. 4 shows our DS learned on 2D data [59]. We use a RBF kernel with  $l = 0.3$ , the KMP is initialized from a GMM with 5 Gaussians sampled at the input data points and *stabilizing policy* with  $\boldsymbol{\Sigma} = \operatorname{diag}(0.1, 0.1)$ . We show the advantages of this KMP-based policy over GPs in Section VIII-C.

#### C. Control Law for DS-based Virtual Fixtures

We use a proportional control law to compute wrenches

$$\mathbf{w}_{\text{VF},i} = \mathbf{D}_{\text{VF},i}(\dot{\mathbf{x}}_{\text{VF},i} - \dot{\mathbf{x}}_{\text{ee}}) \quad (32)$$

with end effector velocity  $\dot{\mathbf{x}}_{\text{ee}}$  and VF velocity  $\dot{\mathbf{x}}_{\text{VF},i}$  ( $\boldsymbol{\mu}_{\text{DS}}$  from (25)) in  $\mathcal{T}_{\mathbf{x}_{\text{ee}}}\mathcal{M}$  and a constant damping  $\mathbf{D}_{\text{VF},i}$ . Note that (32) can be derived from (4) by setting  $\mathbf{K}_{\text{VF},i} = \mathbf{0}$ .

The fixture wrench  $\mathbf{w}_{\text{VF},i}$  is expressed in the cotangent space  $\mathcal{T}_{\mathbf{x}_{\text{ee}}}^*\mathcal{M}$ . As detailed in Section IV-A,  $\mathbf{w}_{\text{VF},i}$  and the associated covariance  $\boldsymbol{\Sigma}_{\text{VF},i}$  have to be transformed to the (co)tangent space of  $\mathbb{R}^3 \times \mathcal{S}^3$  which allows for a natural arbitration between different velocity fixtures and other types of VFs.

## VI. POSITION-BASED TRAJECTORY FIXTURES: LEARNING, ARBITRATION AND AUTOMATION

Position-based trajectory Virtual Fixtures for **precise guidance** compute a probabilistic attractor from the robot state  $\mathbf{x}_{\text{ee}}$

$$p(\mathbf{x}_{\text{PB}}|\mathbf{x}_{\text{ee}}) = \mathcal{N}(\mathbf{x}_{\text{PB}}|\boldsymbol{\mu}_{\text{PB}}, \boldsymbol{\Sigma}_{\text{PB}}) \quad (33)$$

This formulation requires both a probabilistic trajectory as well as a distance function for mapping the end effector pose  $\mathbf{x}_{\text{ee}}$  to the closest pose on the trajectory. To benefit from the different manifolds  $\mathcal{M}$  introduced in Section III-A, we show the extension of [8] from the manifold  $\mathbb{R}^3 \times \mathcal{S}^3$  to  $\mathcal{M}$ . Furthermore, we introduce an automation of this fixture in Section VI-D. The probabilistic wrench of each of  $N_{\text{PB}}$  concurrently active trajectory fixtures calculated through variable impedance control (Section IV-B) is again combined with all other fixtures through the arbitration (Section IV-A).

### A. Learning of Trajectory Fixtures on different Manifolds $\mathcal{M}$

We start from a dataset of trajectories  $\{t_i, \mathbf{x}_i\}_{i=1}^N$  containing demonstrations with time  $t \in \mathbb{R}^1$  and pose  $\mathbf{x} \in \mathcal{M}$  for each of the  $N_{\text{PB}}$  fixtures. Dynamic time warping (DTW) [60] then allows us to align the individual demonstrations in  $t \in [0, 1]$  to encode them in a GMM (5) with  $M$  components. To benefit from the properties of different manifolds  $\mathcal{M}$ , we use the square root of the distance function defined in (2) with  $\mathbf{A} = \mathbf{I}$  as distance measure between the two poses  $\mathbf{x}_j$  and  $\mathbf{x}_k$  in the DTW calculation. This for example allows us to learn trajectories in cylindrical coordinates  $\mathcal{M}_2$ , see Section VIII-D for an evaluation. The effect of this distance measure for Cartesian and cylindrical coordinate systems is shown in Fig. 22. The result of DTW is comparable to the introduction of a phase variable [22]. Using GMR, we condition the GMM on time  $t$  to obtain probabilistic poses  $p(\mathbf{x}|t)$  (6).

### B. On-Manifold Attractor Point Calculation

For impedance control, a single attractor point as in (7) is required. In the Euclidean case, a closed form solution exists for extracting this point on a time-based probabilistic trajectory [21]. As on-manifold Gaussian operations require iterations with a variable number of steps [47], they are not well suited for real-time control. We therefore extract a trajectory from the conditional distribution  $p(\mathbf{x}|t)$  by calculating  $\{\boldsymbol{\mu}_n, \boldsymbol{\Sigma}_n\}_{n=1}^N$  for  $N$  equally spaced samples of  $t \in [0, 1]$ . This trajectory is then sent to the real-time controller for on-manifold interpolation of the attractor  $\mathbf{x}_{\text{PB}}$  as detailed in Section F and variable stiffness control (Section IV-B) to calculate  $\mathbf{w}_{\text{VF},i}$ .

### C. Distance-based Covariance Adaptation

The covariance  $\boldsymbol{\Sigma}_{\text{PB}}$  is used for variable impedance control (Section IV-B) and for the arbitration with other fixtures (IV-A). By default, the covariance matrix only depends on the closest point of the trajectory, thus only modeling aleatoric uncertainty, and does not incorporate the end effector distance to the trajectory. This results in large wrenches  $\mathbf{w}_{\text{VF},i}$  when the end effector  $\mathbf{x}_{\text{ee}}$  is far away from the fixture even though the trajectory might not be valid anymore for the current robot pose. We therefore propose to adapt the original covariance output of the fixture by a linear distance-based scaling of the precision matrix  $\mathbf{P}_{\text{PB}} = \boldsymbol{\Sigma}_{\text{PB}}^{-1}$  to  $\hat{\mathbf{P}}_{\text{PB}} = s \cdot \mathbf{P}_{\text{PB}}$  using

$$s = \begin{cases} 1, & d < d_{\min} \\ 1 - \frac{d_{\mathcal{M}}^{\mathcal{M}}(\mathbf{x}_{\text{PB}}, \mathbf{x}_{\text{ee}}) - d_{\min}}{d_{\max} - d_{\min}}, & d_{\min} \leq d \leq d_{\max} \\ 0, & d > d_{\max} \end{cases} \quad (34)$$

with the Mahalanobis distance  $d_{\mathcal{M}}^{\mathcal{M}}(\mathbf{x}_{\text{PB}}, \mathbf{x}_{\text{ee}})$  between end effector  $\mathbf{x}_{\text{ee}}$  and attractor  $\mathbf{x}_{\text{PB}}$  weighted by the precision matrix  $\mathbf{P}_{\text{PB}}$ . The parameters  $d_{\min}$  and  $d_{\max}$  determine the distances at which the precision matrix scaling starts and ends, respectively. Using the Mahalanobis distance takes the influence of specific DoFs into account, thus leaving the fixture active for longer in directions with high uncertainty. This is relevant to exploit the variable stiffness formulation (Section IV-B) where those directions get much lower stiffnesses, thus allowing the operator to move more freely. The resulting behaviour is showcased in Section VIII-G.

### D. Automating the Fixture

As the position-based fixture is derived from a time-driven motion, we can compute a preferred direction along the trajectory. Inspired by [36], we calculate the current direction

$$\boldsymbol{\delta} = \boldsymbol{\mu}_{j+1, \text{pos}} - \boldsymbol{\mu}_{j, \text{pos}} \quad (35)$$

where  $\boldsymbol{\mu}_{j, \text{pos}}$  and  $\boldsymbol{\mu}_{j+1, \text{pos}}$  are the  $\mathbb{R}^3$  positions of the interpolation points of the fixture. Subsequently, we normalize  $\boldsymbol{\delta}$  to  $\tilde{\boldsymbol{\delta}} = \frac{\boldsymbol{\delta}}{\|\boldsymbol{\delta}\|}$ . The same velocity controller as employed for DS based fixtures (Section V-C) is used to calculate an automation wrench  $\mathbf{w}_{\text{VF}, \text{aut}, i}$  from  $\tilde{\boldsymbol{\delta}}$ . The resulting wrench is then added to the wrench of the impedance controller (4)

$$\tilde{\mathbf{w}}_{\text{VF}, i} = \mathbf{w}_{\text{VF}, i} + \mathbf{w}_{\text{VF}, \text{aut}, i}. \quad (36)$$

## VII. GEOMETRIC VISUAL SERVOING FIXTURE

Probabilistic visual servoing VFs introduced in [8] for **very precise guidance** model the attractor based on visual input I

$$p(\mathbf{x}_{\text{VS}}|\mathbf{I}) = \mathcal{N}(\mathbf{x}_{\text{VS}}|\boldsymbol{\mu}_{\text{VS}}, \boldsymbol{\Sigma}_{\text{VS}}). \quad (37)$$

We consider  $N_{\text{VS}}$  concurrently active visual servoing VFs, each modeling the combination of  $M$  individual fixtures, one for every probabilistic visual detection  $p_m(\mathbf{x}_{\text{VS}}|\mathbf{x}_{\text{ee}}) = \mathcal{N}(\mathbf{x}_{\text{VS}}|\boldsymbol{\mu}_m, \boldsymbol{\Sigma}_m)$ , depending on the end effector pose  $\mathbf{x}_{\text{ee}}$ . We assume that the uncertainty given by the visual detection incorporates uncertainties resulting from e.g. ambiguous or occluded detections. A MoE model [51], [61] allows to model the fixture as a multi-modal distribution

$$p(\mathbf{x}_{\text{VS}}|\mathbf{x}_{\text{ee}}) = \sum_{m=1}^M \hat{h}_m(\mathbf{x}_{\text{ee}}, \boldsymbol{\mu}_m) p_m(\mathbf{x}_{\text{VS}}|\mathbf{x}_{\text{ee}}). \quad (38)$$

Variable impedance control (Section IV-B) is used to calculate a wrench for each of the  $N_{\text{VS}}$  fixtures which is then fused with all other fixtures through the arbitration (Section IV-A).

### A. Geometry-aware Mixture of Experts Gating Functions

In [62], the *gating function*  $h_m$  computes the influence of each expert based on the distance between expert and end effector  $\mathcal{M}_1$ . Using the geometry-aware distance function (2), we can generalize to manifolds  $\mathcal{M}_i$  defined in Section III-A

$$h_m(\mathbf{x}_{\text{ee}}, \boldsymbol{\mu}_m) = \exp\left(-\frac{1}{2}d_{\mathbf{L}}^{\mathcal{M}}(\mathbf{x}_{\text{ee}}, \boldsymbol{\mu}_m)\right) + \gamma \quad (39)$$

where  $\gamma$  is a regularization factor and the hyperparameter  $\mathbf{L} = \text{diag}(l_0^2, l_1^2, l_2^2, l_{wx}^2, l_{wy}^2, l_{wz}^2)^{-1}$  allows to specify the relevance of each direction. For  $\mathcal{M}_1$ ,  $l_0$ ,  $l_1$  and  $l_2$  correspond to  $x$ ,  $y$  and  $z$ . For  $\mathcal{M}_2$ ,  $l_0$  and  $l_1$  scales angular DoF and radius  $r$ . In case of  $\mathcal{M}_3$ ,  $l_0$  and  $l_1$  weigh the two angular DoFs and  $l_2$  radius  $r$ . When far from all detections,  $\gamma$  assigns equal weights for each expert, reflecting the overall uncertainty of all detections.

Similarly to [8], we compute a unimodal distribution from (38) via moment matching resulting in mean  $\boldsymbol{\mu}_{\text{VS}}$  and covariance  $\boldsymbol{\Sigma}_{\text{VS}}$ , used by the impedance controller (4) with variable stiffness (Section IV-B). The fixture wrench is again combined with all other fixture wrenches through the arbitration (Section IV-A).

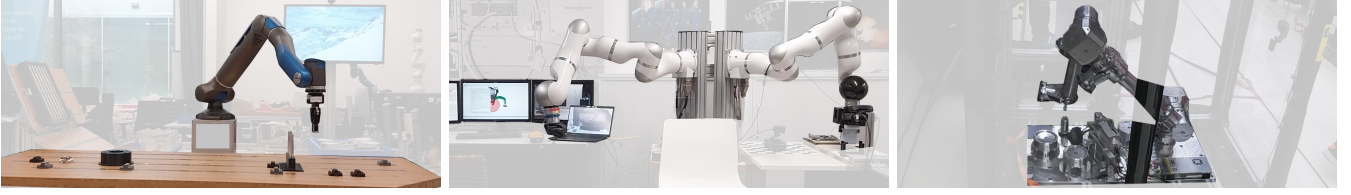


Fig. 5: A torque-controlled 7-DoF manipulator (left) is used in *hand-guided* mode for evaluating individual fixtures in Sections VIII-A to VIII-C, as well as their combinations in Sections VIII-F and VIII-G. A dual arm setup with two torque-controlled 7-DoF manipulators (center) is used for evaluating the fixtures in a *teleoperation* task in Section VIII-F. A space-ready, 4-DoF robot arm (right) is used with *fully automated* fixtures (Sections VIII-C to VIII-E).

## B. Geometric Expert Customization

While the *gating function*  $h_m$  of [8] naturally extends to other manifolds, the expert customization also found therein needs to be flexibilised and formalized.

1) *Zero force along insertion axis*: We assume that the insertion that should be controlled by the operator is to be performed along one DoF of the chosen manifold. Therefore, the stiffness in the corresponding row and column of  $\mathbf{K}$  is set to zero to not generate any forces along this axis and allow the operator full control over the insertion.

2) *Deadzones*: In the vicinity of a connector, the operator should receive strong guidance. This can be achieved by modifying  $\text{Log}_{\mathbf{x}_{ee}}^{\mathcal{M}}(\boldsymbol{\mu}_m)$ , setting its entries to zero for distances smaller than a predefined radius and scaling it for larger distances. We use a length vector  $\mathbf{l}_{\text{dead}}$  to deform the difference vector as well as the scalar deadzone value  $r_{\text{dead}}$  to calculate the modified logarithm  $\text{Log}'_{\mathbf{x}_{ee}}{}^{\mathcal{M}}(\boldsymbol{\mu}_m)$  (Section G). The modified value is then used in the gating function (39).

3) *Expert Initialization*: As in [8], we initialize the MoE with an additional expert at the end effector pose with high covariance. This additional expert ensures that the fixture does not generate forces outside its valid region. It is parameterized with length scale  $\mathbf{l}_{\text{dead,add}}$  and dead zone  $r_{\text{dead,add}}$ , calculating the modified difference  $\text{Log}'_{\mathbf{x}_{ee}}{}^{\mathcal{M}}(\boldsymbol{\mu}_m)$  (Section G). Its influence factor  $h_{M+1}$  is then calculated as in [8]

$$h_{M+1}(\mathbf{x}_{ee}, \mathbf{x}_{\text{targ}}) = 1 - \exp\left(-\frac{1}{2} d'_{\mathbf{L}_{\text{add}}}{}^{\mathcal{M}}(\mathbf{x}_{ee}, \boldsymbol{\mu}_m)\right), \quad (40)$$

where  $\mathbf{L}_{\text{add}} = \text{diag}(\mathbf{l}_{\text{add}})$  is the length vector for the additional expert,  $\mathbf{x}_{\text{targ}}$  the expected mean of the experts and the modified  $\text{Log}'_{\mathbf{x}_{ee}}{}^{\mathcal{M}}(\boldsymbol{\mu}_m)$  is used in  $d'_{\mathbf{L}_{\text{add}}}{}^{\mathcal{M}}(\mathbf{x}_{ee}, \boldsymbol{\mu}_m)$ .

## VIII. EVALUATION

Our framework is implemented on three different robotic systems (Fig. 5) in different *automation levels* as well as different *interaction modes* (Table II). The VFs are implemented on standard computers using Simulink and C++ code running in hard real time at the robot's control rate of up to 8 kHz. As first system (left image), we use a torque-controlled 7-DoF manipulator in *hand-guided mode*, i.e. an operator directly interacts with the arm, representing human-robot collaboration in a factory context. On this robot, we evaluate components of our framework as well as use cases in *manual* and *semi-automated* mode. To emulate a space application, we use a dual arm setup with two torque-controlled 7-DoF manipulators (middle image) where one robot arm is used as haptic input

TABLE II: AUTOMATION LEVELS AND INTERACTION MODES.

Experiment	Automation level	Interaction mode
Section VIII-A	manual	hand-guided
Section VIII-B	manual	hand-guided
Section VIII-C	fully automated	without
Section VIII-D	fully automated	without
Section VIII-E	fully automated	without
Section VIII-F	semi-automated	teleoperation & hand-guided
Section VIII-G	semi-automated	hand-guided

device and the other as remote robot to test the fixtures in a *teleoperation* setup in *semi-automated* mode. Finally, we use a space-ready, 4-DoF robot arm (right image) *without* interaction in *fully automated* mode. Implementation on a space-grade computer showcases applicability of our method on space hardware. This setup is designed to be tested in outer space; experiments in this paper were conducted on a parabolic flight.

We start with a *qualitative* evaluation of our novel variable stiffness formulation (Section IV-B). We demonstrate coupled translational and rotational DoFs in Section VIII-A and low stiffness along DoFs of  $\mathcal{M}_3$  in Section VIII-B. Next, in Section VIII-C, we compare our novel DS-based VF with a GP baseline, *quantifying* how much repeated executions differ in their trajectories. Finally, we *quantify* the repeatability of the automated position-based fixture (Section VI) over multiple fully autonomous executions in Section VIII-D.

Leveraging the arbitration (Section IV-A), we combine different types of fixtures. We first combine DS- and position-based VFs in *fully automated* execution (Section VIII-E). Next, we combine DS-based and visual servoing fixtures to achieve automation where possible with human interaction where required (Section VIII-F). Finally, we use all fixture types (Section VIII-G) where we also perform a validation of the usability of the framework with 6 expert users.

### A. Visual Servoing Fixture with Coupled Variable Stiffness

Figure 6 shows the use case of robotic chess playing with the visual servoing fixture ( $N_{\text{VS}} = 1$ ,  $M = 2$ ) on a chess field with size of 40 cm  $\times$  40 cm. Two chess figure detections with covariance  $\boldsymbol{\Sigma} = 5 \times 10^{-6} \cdot \mathbf{I}_6$  and a rotation difference of 180° are simulated on fields 1a and 8h. With parameters  $l_x = l_y = l_z = 0.06$ ,  $l_{wx} = l_{wy} = l_{wz} = 0.2$ ,  $\gamma = 1 \times 10^{-20}$ , we get an in-between attractor point with a precision matrix coupling translational and rotational DoFs

$$\mathbf{P} = \begin{bmatrix} 2.0 \times 10^5 & 2.4 \times 10^3 & -1.8 \times 10^1 & 1.4 \times 10^{-1} & -1.4 \times 10^{-1} & -2.2 \times 10^4 \\ 2.4 \times 10^3 & 2.0 \times 10^5 & 1.8 \times 10^1 & -1.4 \times 10^{-1} & 1.4 \times 10^{-1} & 2.2 \times 10^4 \\ -1.8 \times 10^1 & 1.8 \times 10^1 & 2.0 \times 10^5 & 1.0 \times 10^{-3} & -1.0 \times 10^{-3} & -1.6 \times 10^2 \\ 1.4 \times 10^{-1} & -1.4 \times 10^{-1} & 1.0 \times 10^{-3} & 2.0 \times 10^5 & -4.0 & 1.2 \\ -1.4 \times 10^{-1} & 1.4 \times 10^{-1} & -1.0 \times 10^{-3} & -4.0 & 2.0 \times 10^5 & -1.3 \\ -2.2 \times 10^4 & 2.2 \times 10^4 & -1.6 \times 10^2 & 1.2 & -1.3 & 4.8 \times 10^3 \end{bmatrix}. \quad (41)$$

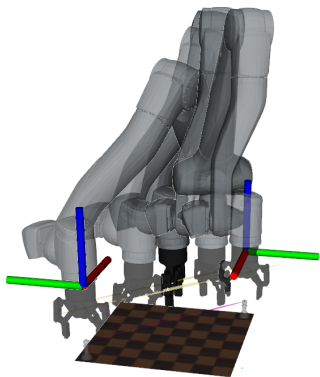


Fig. 6: Visual servoing fixture (Section VII) on  $\mathcal{M}_1$  with two targets with an orientation difference of  $180^\circ$  around the  $z$  axis and position differences both along the  $x$  and  $y$  axis. This leads to a covariance matrix with couplings both inside the positional as well as between positional and rotational DoFs, therefore necessitating a fully populated stiffness matrix.

Our novel variable stiffness formulation (Section IV-B) with  $\lambda_{\text{rot}}^- = \lambda_{\text{trans}}^- = 1000$ ,  $\lambda_{\text{rot}}^+ = \lambda_{\text{trans}}^+ = 2500$ ,  $k_{\text{trans,nom}} = 1000$  and  $k_{\text{rot,nom}} = 40$  computes the stiffness matrix

$$\mathbf{K} = \begin{bmatrix} 1000.0 & * & * & * & * & -111.4 \\ * & 1000.0 & * & * & * & 111.5 \\ * & * & 1000.0 & * & * & -0.8 \\ * & * & * & 40.0 & * & * \\ * & * & * & * & 40.0 & * \\ -111.4 & 111.5 & -0.8 & * & * & 24.8 \end{bmatrix}, \quad (42)$$

with entries  $* < 1e-3$ , allowing the operator to freely move along the geodesic between both detections. This geodesic, unlike previous variable stiffness formulations, couples translational movement with an orientation change which can also be seen in the supplementary video and is further discussed in Section IX-C. Note that unlike in [8], the operator is not always attracted to one of the detections as the choice of length scales assigns approximately equal weights to both detections when the end effector is located in between.

### B. Position-based Fixture with Variable Stiffness

Fig. 7 shows the position-based trajectory fixture ( $N_{\text{PB}} = 1$ ,  $M = 2$ ) used for a pointing task on the spherical manifold  $\mathcal{M}_3$  learned from four demonstrations of a movement towards the coordinate origin. The resulting fixture exhibits a large covariance around the two rotational DoFs of  $\mathcal{S}^2$  (visualized by the turquoise Gaussian at the end effector), resulting in a precision matrix with small entries  $P_{1,1}$ ,  $P_{2,2}$  and  $P_{3,3}$

$$\mathbf{P} = \begin{bmatrix} 344 & -23 & -109 & -110 & 280 & -166 \\ -23 & 46 & 58 & 133 & 48 & 31 \\ -109 & 58 & 723 & -74 & -22 & 78 \\ -110 & 133 & -74 & 794 & 58 & 112 \\ 280 & 48 & -22 & 58 & 533 & -81 \\ -166 & 31 & 78 & 112 & -81 & 94 \end{bmatrix}. \quad (43)$$

With  $\lambda_{\text{rot}}^- = 0.5$ ,  $\lambda_{\text{rot}}^+ = 1.5$ ,  $\lambda_{\text{trans}}^- = 400$ ,  $\lambda_{\text{trans}}^+ = 500$ ,  $k_{\text{trans,nom}} = 500$  and  $k_{\text{rot,nom}} = 40$ , we obtain the stiffness

$$\mathbf{K} = \begin{bmatrix} 5 & -2 & -20 & * & 2 & -3 \\ -2 & * & 7 & * & * & 1 \\ -20 & 7 & 74 & -3 & -9 & 12 \\ * & * & -3 & 40 & * & * \\ 2 & * & -9 & * & 41 & -1 \\ -3 & 1 & 12 & * & -1 & 42 \end{bmatrix} \quad (44)$$

with entries  $* < 1$ . Compared to the nominal stiffness matrix  $\mathbf{K}_{\text{nom}} = \text{diag}(80, 80, 500, 40, 40, 40)$  at  $r = 16$  cm, these

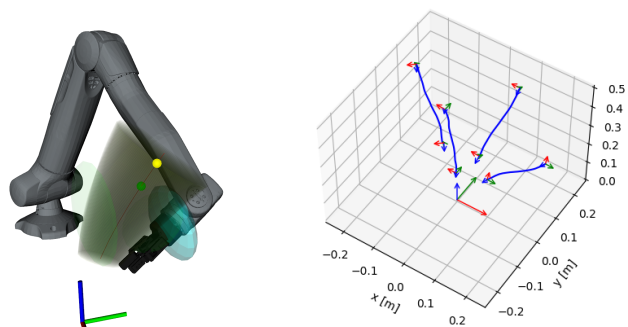


Fig. 7: Position-based fixture (Section VI) on the spherical manifold  $\mathcal{M}_3$  ( $\mathcal{S}^2 \times \mathbb{R}^1 \times \mathcal{S}^3$ ) with variable stiffness learned from four demonstrations (right side). The trajectory with red mean and covariance visualized as yellow tube consists of  $M = 2$  Gaussians plotted as green ellipsoids. The green dot on the red mean trajectory depicts the attractor point computed using the Mahalanobis distance ( $\mathbf{A} = \mathbf{\Sigma}^{-1}$  in (2)) while the yellow dot would be computed using a non-weighted distance metric ( $\mathbf{A} = \mathbf{I}$  in (2)).

downscaled values allow a human operator to freely move around the object centered at the coordinate origin while always pointing at it which is e.g. valuable for inspection tasks.

Crucial for this fixture is also the correct attractor point selection through (60), (61). It ensures that the attractor point stays the same when moving along a zero-force direction extracted by the variable impedance control Section IV-B. This is achieved by computing both attractor point as well as stiffness from the precision matrix  $\mathbf{P}_{\text{VF}} = \mathbf{\Sigma}_{\text{VF}}^{-1}$ , ensuring that length scales in the distance calculation correspond to stiffness scales as visualized in Fig. 7.

### C. Probabilistic Dynamical System Virtual Fixtures

We evaluate the novel DS based VF (Section V) on two DS policies consisting of transport motions from right to left in the robot's workspace (Figs. 8 and 9). The right motion consists of five demonstrations diverging towards the middle of the workspace while the left motion consists of four demonstrations which are very close together. For evaluation purposes we compare the performance of GP and KMP representations on  $\mathcal{M}_1$ . To limit the amount of data used in the models, the recorded trajectories are subsampled at a distance of 5 cm before calculating the velocities based on time differences.

Through empirical trials we found that with human interaction, policies using a full pose  $\mathbf{x} \in \mathcal{M}$  as input and outputting a velocity  $\dot{\mathbf{x}} \in \mathbb{R}^6$  lead to non-smooth behavior due to the curse of dimensionality. When a human perturbs the robot's orientation, the epistemic uncertainty of the learned policy increases, activating the *stabilizing policy*. This policy only acts towards the closest pose  $\mathbf{x}$  without forward motion component  $\dot{\mathbf{x}}$ , therefore halting the evolution of the DS. Splitting the DS in two components, one with position input  $\mathbf{x}_{\text{pos}} \in \mathbb{R}^3$  and output velocity  $\dot{\mathbf{x}}_{\text{pos}} \in \mathbb{R}^3$  and the other with the full pose as input  $\mathbf{x} \in \mathcal{M}$  and rotational velocity  $\boldsymbol{\omega} \in \mathcal{T}_{\mathbf{x}_{\text{rot}}}^{\mathcal{S}^3}$  as output, this problem can be mitigated. The full set of velocity policies for this experiment therefore consists of  $N_{\text{DS}} = 5$  concurrently active policies: one *stabilizing policy* and two policies each for the left and the right side of the motion. All policies are fused through the arbitration (Section IV-A).

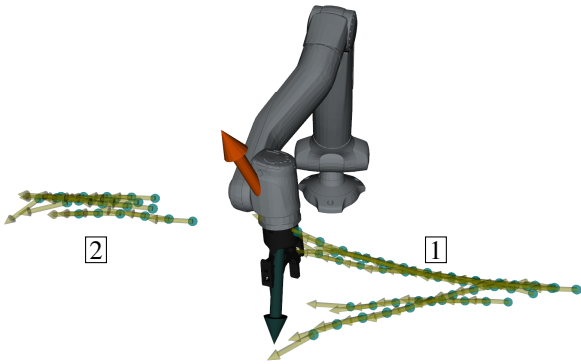


Fig. 8: DS based VF using a GP model. Yellow arrows starting at turquoise dots visualize known velocities. The green arrow corresponds to the output of the velocity policy  $\boxed{1}$  on the right side while the red arrow depicts the velocity output of the velocity policy  $\boxed{2}$ . Both counteract each other due to erroneous velocity measurements at the borders of the dataset, leading to a stuck evolution of the system unable to transition from  $\boxed{1}$  to  $\boxed{2}$ .

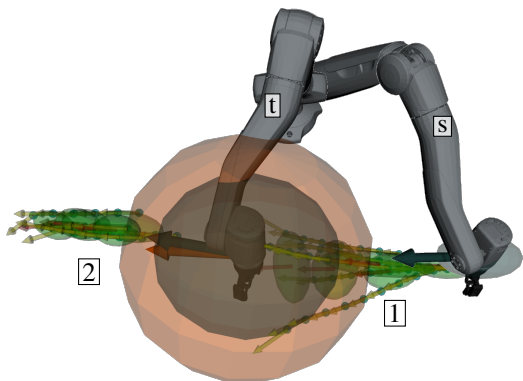


Fig. 9: DS-based VF using a KMP model for the robot in start  $\boxed{s}$  and transition  $\boxed{t}$  configurations. Yellow arrows starting at turquoise dots visualize known velocities. Green Gaussians depict the positional uncertainty of the underlying GMM with mean velocity as red arrows. The dark green Gaussian with green velocity arrow at the end effector represents policy  $\boxed{1}$ . The orange-red Gaussian with red velocity arrow visible in  $\boxed{t}$  configuration corresponds to policy  $\boxed{2}$ . In  $\boxed{t}$ , a smooth transition between policies is happening. In  $\boxed{s}$  configuration, no output for policy  $\boxed{1}$  is visible due to its high uncertainty.

In Fig. 8, policies encoded using a GP are visualized. For the positional GP we use a RBF kernel (27) with  $l = 0.1$  and for the rotational GP  $l = 0.03$ . We set both process variances to  $\lambda = 0.01$ . As shown in the supplementary video, the evolution of the DS closely follows the demonstration trajectories but fails to capture their variance, both for left and right policies. Furthermore, the velocities generated by the GP, as seen in Fig. 10, exhibit abrupt changes, suggesting limited smoothness in the generated trajectories. A higher value of  $\lambda$  could smoothen the prediction of the process, which would however have a global effect and not be restricted to the demonstrated high-variance zone. The robot also fails to transition between policies, halting at the final pose of policy  $\boxed{1}$  and requiring operator input to proceed.

Fig. 9 shows the same data encoded in a DS using a KMP based on a GMM with  $M = 5$  Gaussians with hyperparameters  $\lambda = 0.05$ ,  $\lambda_c = 10$ ,  $\alpha = 0.1$  and  $l = 0.1$

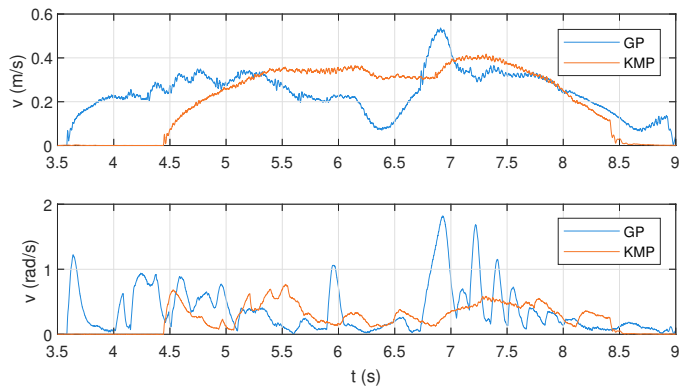


Fig. 10: Translational (upper plot) and rotational (lower plot) velocities observed during a human interaction with GP- and KMP-based velocity fixtures. With the KMP, both rotational velocities as well as the transition from policy  $\boxed{1}$  to  $\boxed{2}$  at  $t = 6.5$  s are much smoother compared to the GP.

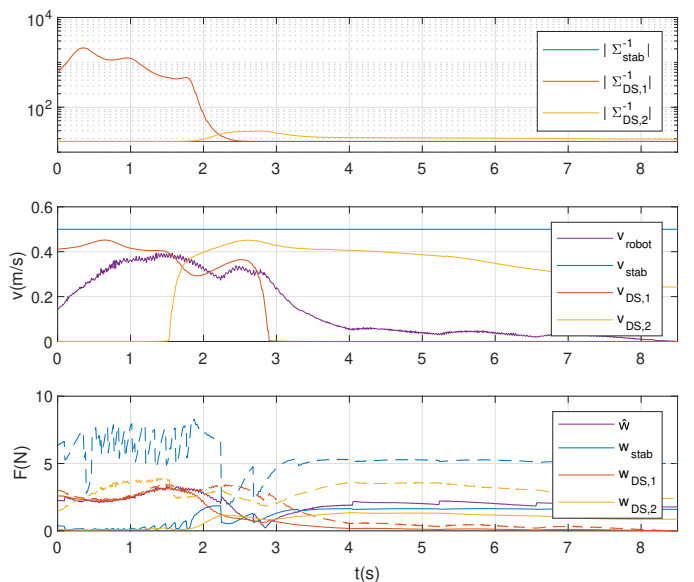


Fig. 11: Norm of covariances (**top**), target velocities (**middle**), raw (dashed,  $w_{VF,i}$ ) and arbitrated (solid lines,  $\sum_{VF} \Sigma_{VF,i}^{-1} w_{VF,i}$  resp.  $\hat{w}$ , see (16)) fixture forces (**bottom**) of the *stabilizing policy* and learned KMP-DS.

in the RBF kernel for the positional respectively  $l = 0.03$  for the rotational KMP. The KMP allows to encode a small covariance at  $\boxed{s}$  and a bigger covariance at  $\boxed{t}$  for the right motion policy. This also enables a system evolution from right to left policy where the GP-based policy failed. Unlike the previous model, the learned covariance permits smoother motion in the high-variance region of the right policy, allowing the robot to deviate from the demonstrations when appropriate, as also seen in the supplementary video. Furthermore, a much smoother velocity profile is obtained (Fig. 10). The arbitration (Section IV-A) plays a key role in coordinating the *stabilizing policy* and the learned policies which is shown for the position components in Fig. 11. First, DS  $\boxed{1}$  dominates the execution, then followed by a mix of DS  $\boxed{2}$  and the *stabilizing policy* as can be seen from arbitrated forces which sum to  $\hat{w}$  (16). The motion converges towards the end of policy  $\boxed{2}$ , when learned and *stabilizing policy* as well as robot friction cancel each other. Over 5 repeated executions of the KMP-based policy,

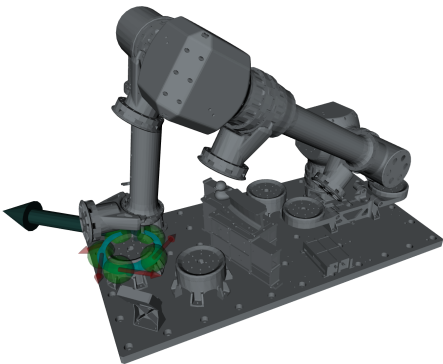


Fig. 12: Dynamical system VF on the space robot setup. A repeating motion in  $S^1 \times \mathbb{R}^2$  around the launch lock is overlaid with a local policy exerting a force perpendicular to the launch lock. The 5 green ellipsoids visualize the position-based covariances of the underlying GMM model with the red arrows depicting its velocities. The green arrow in the back visualizes the current output of the velocity fixture along the launch lock.

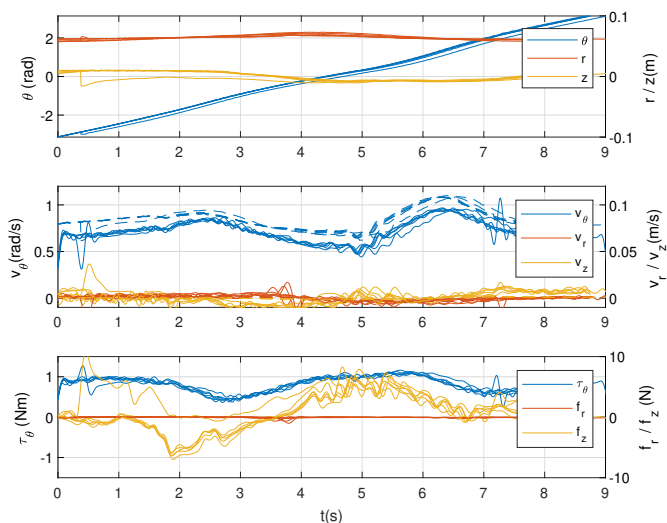


Fig. 13: Robot poses on  $\mathcal{M}_2$  (**top**), desired (dashed) as well as measured velocities (**middle**) and computed forces (**bottom**) for 6 repetitions of the circular motion shown in Fig. 12 during the 0g phase of the parabolic flight. One trajectory deviates from the rest with a disturbance in  $z$  caused by starting the robot already before the 0g phase, but recovers over time as the *stabilizing policy* outputs a desired velocity and thus force in  $+z$  direction.

we obtain a standard deviation of  $(0.006, 0.012, 0.006)$  m and  $(0.012, 0.005, 0.012)$  rad between end effector poses as well as  $(0.007, 0.011, 0.008)$   $\frac{\text{m}}{\text{s}}$  and  $(0.026, 0.019, 0.053)$   $\frac{\text{rad}}{\text{s}}$  for velocities at the same time point. Note that an error between desired and measured velocity as visible in Fig. 11 is required for the proportional controller (32) to generate a wrench.

We encode repetitive motions in the same policy representation (Fig. 12). This fixture ( $N = 1$ ) is learned on  $\mathcal{M}_2$  from a demonstration of circling the launch adapter ring of the space robot setup 4 times. It is encoded in a KMP based on a GMM with  $M = 5$  Gaussians with hyperparameters  $\lambda = 0.1$ ,  $\lambda_c = 10$ ,  $\alpha = 0.1$ ,  $h = 1$  and  $l = 0.03$ . We use the arbitration to overlay a wrench pointing along  $-r$  with

$$\mathbf{w} = (0, -10 \text{ N}, 0)^\top, \quad \Sigma = \text{diag}(0, 2 \times 10^{-4} \text{ m}^2, 0). \quad (45)$$

We evaluate the motion both on ground as well as under 0g conditions, controlling only the position of the

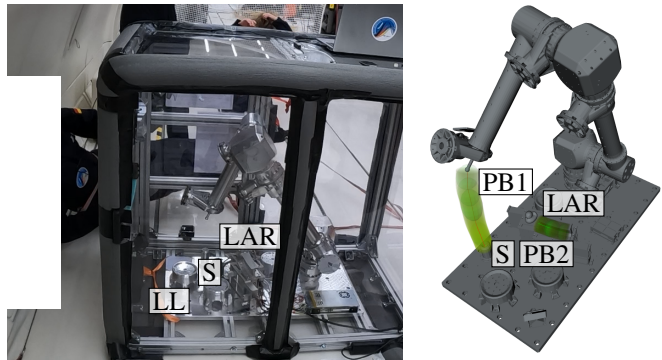


Fig. 14: Left image: The space robot setup approaching the spring [S] using an automated position-based fixture during the 0g phase of a parabolic flight. Also shown are the launch adapter ring segment [LAR] and the launch lock [LL]. Right image: [PB1] denotes a position-based fixture for approaching and pressing the spring assembly [S] while [PB2] shows the second position-based fixture for the robot moving along the launch adapter ring segment [LAR].

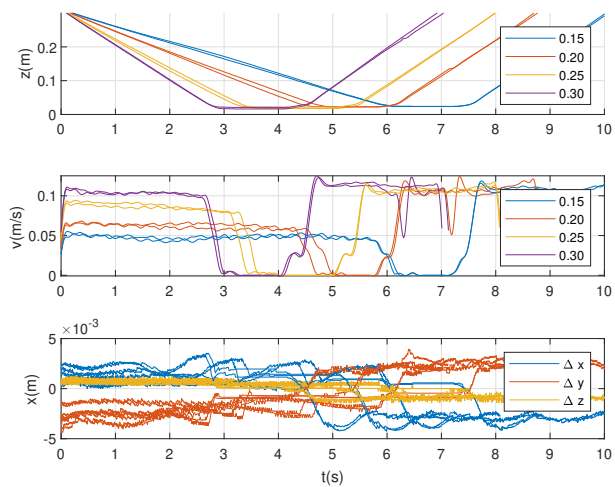


Fig. 15: Repeated execution of the spring pressing task (Fig. 14 with different velocities). Differences between the setpoint velocities of  $0.15 \frac{\text{m}}{\text{s}}$ ,  $0.2 \frac{\text{m}}{\text{s}}$ ,  $0.25 \frac{\text{m}}{\text{s}}$  and  $0.3 \frac{\text{m}}{\text{s}}$  for pressing - for retracting, we always use  $-0.3 \frac{\text{m}}{\text{s}}$  - and the velocities visible in the middle plot are caused by friction in the joints that has to be overcome by the velocity controller with a gain of  $150 \frac{\text{N}}{\text{m}}$ .

robot. Fig. 13 shows trajectories, computed forces, desired and measured velocities of 6 repetitions of the policy on the parabolic flight; the same plot on ground looks very similar and is therefore omitted. We obtain a standard deviation of  $(0.069 \text{ rad}, 0.001 \text{ m}, 0.003 \text{ m})$  for positions as well as of  $(0.493 \frac{\text{rad}}{\text{s}}, 0.013 \frac{\text{m}}{\text{s}}, 0.018 \frac{\text{m}}{\text{s}})$  for velocities during flight as well as of  $(0.055 \text{ rad}, 0.001 \text{ m}, 0.001 \text{ m})$  and  $(0.207 \frac{\text{rad}}{\text{s}}, 0.007 \frac{\text{m}}{\text{s}}, 0.007 \frac{\text{m}}{\text{s}})$  on ground. Higher deviations during flight can be explained by disturbances induced by stopping the robot in between the 0g phases. Overall small standard deviations in both experiments show that despite only aiming for **coarse guidance**, without external perturbations, the repeatability of the DS based fixture is remarkably high.

#### D. Automated Position-based Fixtures

For higher precision motions, where following a defined trajectory is required, an automated position-based trajectory fixture (Section VI) is well suited. We first demonstrate this fixture on the fully automated task of pressing a spring on the

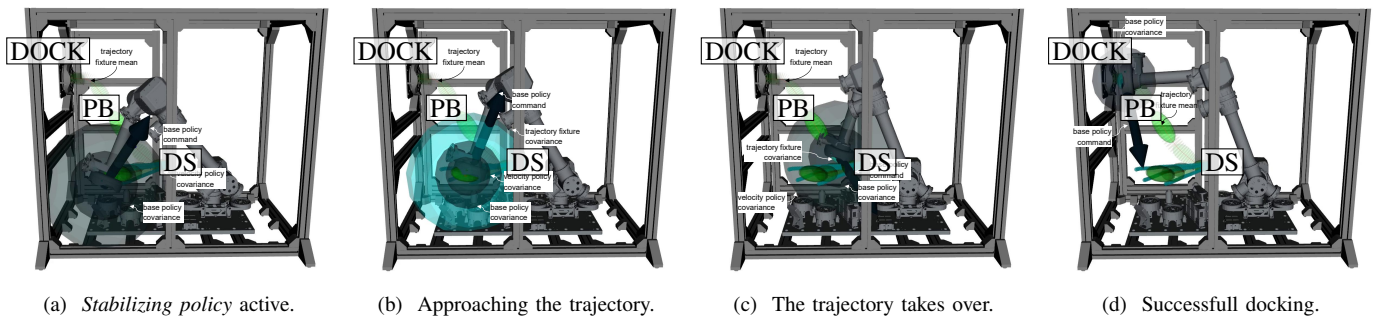


Fig. 16: DS-based VF  $\overline{\text{DS}}$  combined with a position-based fixture  $\overline{\text{PB}}$  on the space robot setup. The DS-based VF guides the robot towards the start of the automated position-based fixture performing a docking of the interface mounted at the end effector to the interface mounted on the rack  $\overline{\text{DOCK}}$ .

space robot setup, again only controlling the position, with the pin end effector of the robot as visualized in Fig. 14. The fixture is learned from two kinesthetic demonstrations of pressing the spring using  $M = 5$  Gaussians. Through GMR, we retrieve a reference trajectory denoted as  $\overline{\text{PB1}}$ . For the evaluation, we first move the robot to the start position of the fixture. During the zero gravity phase of the parabolic flight, we press the spring four times with different velocities as seen in the video and in Fig. 15. During two repetitions of this procedure, we obtain standard deviations of the end effector pose from the attractor point on the fixture of  $(0.002, 0.002, 0.001)$  m both during flight as well as on ground at a constant stiffness of  $3000 \frac{\text{N}}{\text{m}}$ . Those deviations lie in the expected range for the robot’s capabilities and model tuning. Similar results on ground as well as under  $0g$  conditions can be explained by slight errors in the gravity compensation model for the former as well as disturbances during flight for the latter.

Concurrently ( $N_{\text{PB}} = 2$ ), a second position-based fixture  $\overline{\text{PB2}}$  is present in the robot’s workspace. However, thanks to the distance-based covariance adaptation (Section VI-C) only the fixture close to the robot end effector creates forces acting on the robot’s end effector. For activating this second fixture, the robot’s end effector is placed close to the  $\overline{\text{LAR}}$ . There, the second position-based fixture learned from 4 demonstrations on the  $\mathcal{S}^1 \times \mathbb{R}^2$  manifold using  $M = 5$  Gaussians gets activated. The origin of this manifold is placed at the center of the launch adapter ring, thus making the motion along the ring follow a perfect circle with constant radius. As in the previous section, we overlay a probabilistic force of  $-10$  N along the radius of the cylindrical manifold, leading to the robot pressing against the  $\overline{\text{LAR}}$ . The motion is executed both during the  $0g$  phase of the flight as well as on ground. With a standard deviation of the position error of  $(0.001 \text{ rad}, 0.002 \text{ m}, 0.001 \text{ m})$  both during flight and on ground, we achieve a more **precise guidance** than with DS-based fixtures.

### E. Combining Dynamical System and Position-based Fixtures

With the uncertainty-aware probabilistic fusion of fixtures through (16) being at the core of our method, we now combine VFs based on dynamical systems and position-based fixtures on the space robot setup. Fig. 16 shows the scenario of docking the iBOSS “iSSI” interface mounted to the end effector of the space robot with its counterpart mounted to the rack, which we

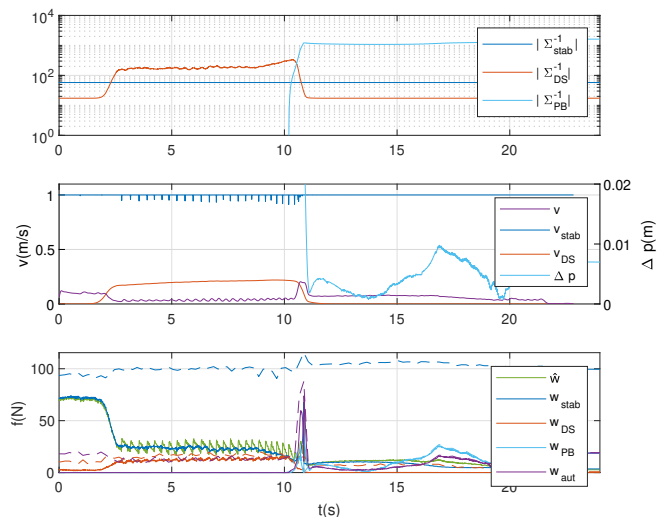


Fig. 17: Norm of covariances (**top**), target velocities and position offset (**middle**), raw (dashed,  $w_{\text{VF},i}$ ) and arbitrated (solid lines,  $\overline{\Sigma}_{\text{VF}} \overline{\Sigma}_{\text{VF},i}^{-1} w_{\text{VF},i}$  resp.  $\hat{w}$ , see (16)) fixture forces (**bottom**) of the *stabilizing policy*, DS-based and trajectory ( $w_{\text{PB}}$ ,  $w_{\text{aut}}$  from VI-D) fixtures used for docking (Fig. 16).

solve by combining a dynamical system VF  $\overline{\text{DS}}$  ( $N_{\text{DS}} = 1$ ) with a position-based trajectory fixture  $\overline{\text{PB}}$  ( $N_{\text{PB}} = 1$ ), both on the  $\mathbb{R}^3$  manifold. The DS is encoded in a KMP based on a GMM with  $M = 5$  Gaussians with hyperparameters  $\lambda = 0.1$ ,  $\lambda_c = 10$ ,  $\alpha = 0.1$ ,  $h = 1$  and  $l = 0.03$ . The trajectory fixture is encoded in a GMM with  $M = 5$  Gaussians. Fig. 16 shows that both fixtures have similar covariance values thanks to the formulation chosen in Section V, allowing for an arbitration of their wrenches even though they are computed from different quantities. This allows to combine a more flexible velocity fixture with the precision coming from a position-based trajectory fixture that can model the exact approach required for a successful mating of the interface. Fig. 17 visualizes fixture target poses and velocities, resulting forces as well as their arbitrated forces summing to  $\hat{w}$  (16). The plot shows that first, the *stabilizing policy* moves the end effector towards the learned DS which is then active until the position-based fixture takes over. Overall, the system behaves as expected even though the *stabilizing policy* is equipped with both non-optimal covariance  $\sigma_{\text{stab}} = 0.04 \text{ m}^2$  and default velocity  $\dot{x}_{\text{stab}} = 1 \frac{\text{m}}{\text{s}}$ , resulting in it also generating forces

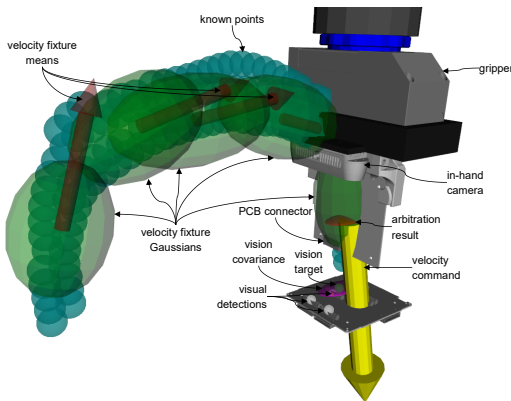


Fig. 18: Semi-automated CubeSat subsystem assembly [6]–[8]: A DS-based fixture takes the operator in the vicinity of the insertion pose where the manual visual servoing fixture takes over. This enables a collaborative automation of the first phase with **coarse** precision while the **very precise** visual servoing fixture with human corrections enables a successful connector insertion.

when only other fixtures should be active.

#### F. Combining Dynamical System and Visual Servoing Fixtures

As explored in previous works [6]–[8], visual input is often required to successfully accomplish the precision requirements of a task. We therefore analyze the task of CubeSat subsystem assembly on the bilateral teleoperation setup with the aim of automating it to the extent possible. To this end, DS-based VFs allow for a flexible but relatively coarse automation. As such, they are well suited for a combination with the very precise visual servoing fixtures combined with human control.

We thus train two velocity fixtures (one for position and one for rotation guidance) resulting in  $N_{DS} = 3$  on the data of [7], modelling it using a KMP with  $\lambda = 0.1$ ,  $\lambda_c = 10$ ,  $\alpha = 0.1$  and  $l = 0.03$  based on a GMM model with each  $M = 5$  Gaussians. The velocity fixtures bring the subsystem to be assembled close to the assembly position where the visual servoing fixture ( $N_{VS} = 1$ ) taken from [8] ensures precise alignment. Figure 18 shows the full set of fixtures.

At the end effector pose visualized in Fig. 18, the covariance of the visual servoing fixture is, for the first time in the experiment, smaller than the covariance of the DS-based fixture. Thus, the velocity output of the latter (yellow arrow) is not guiding the robot anymore. Instead, only the visual servoing fixture is active, reproducing the assistive behaviour introduced in [8], but combining it with the increased flexibility of the novel DS-based fixture. Notably, this enables the robot to begin from any position within its workspace, eliminating the need for initial alignment. Section D describes the teleoperation coupling used in the experiment.

To also show the extension of the visual servoing fixture to the cylindrical manifold  $\mathcal{M}_2$ , we set up an experiment where the task is to move test tubes from a linear holder [H1] to a cylindrical holder [H2] visualized in Fig. 19 with  $N_{VS} = 2$ . To simplify the implementation, we simulate visual measurements for all tube holder positions with  $\Sigma = 2.25 \times 10^{-1} \cdot \mathbf{I}_6$ . For the visual servoing fixture in  $\mathcal{M}_1$ , we use the length scale  $l = (0.006, 0.006, 0.2, 0, 0, 0)$  and a deadzone of 5 mm in the  $xy$ -plane. For the visual servoing fixture in  $\mathcal{M}_2$ , we set the

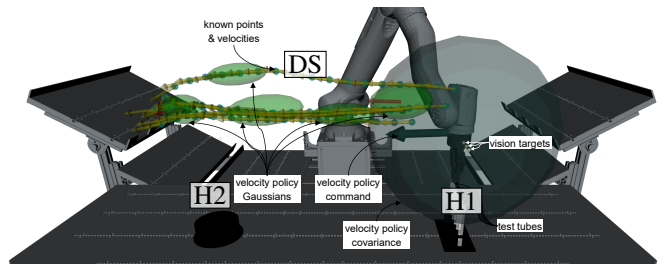


Fig. 19: Combination of dynamical system and visual servoing fixtures on the scenario of transporting test tubes from a linear holder [H1] on the right side to a circular holder [H2] on the left side. The operator is supported by a visual servoing fixture at each holder as well as a dynamical system [DS] supporting with the transportation between both holders.

length scale  $l = (0.1, 0.05, 0.2, 0, 0, 0)$  and use a deadzone of 0.2 rad along the angular DoF. For the DS ( $N_{DS} = 3$ ), we again use a KMP based on a GMM with  $M = 5$  Gaussians with hyperparameters  $\lambda = 0.05$ ,  $\lambda_c = 10$ ,  $\alpha = 0.1$ ,  $h = 1$  and  $l = 0.1$  for positions respectively 0.03 for orientations. This setup allows an operator to easily choose a test tube to pick up through guidance from a visual servoing fixture, transport it to the other holder while the velocity fixture supports with a velocity field and by keeping the tube upright where the other visual servoing fixture eases the placement.

#### G. Semi-Automated Combination of All Fixtures

Finally, we combine position-based, velocity and visual servoing fixtures in one scenario ( $N_{PB} = 1$ ,  $N_{DS} = 3$ ,  $N_{VS} = 1$ ; Fig. 20). The task is to pick up a bottle [B] and place it in the crate [C] supported by a position-based trajectory fixture for picking up the bottle, a velocity fixture for transporting it towards the crate and a visual servoing fixture allowing to select from multiple placement locations.

From 3 demonstrations of picking up the bottle with approaches from different angles we learn a trajectory fixture supported by a GMM with  $M = 2$  Gaussians on the cylindrical manifold  $\mathcal{M}_2$  centered inside the bottle. Due to its high covariance along the angle  $\phi$  of the manifold, the variable stiffness formulation sets a very low stiffness for this DoF, allowing the bottle to be picked up from multiple angles (Fig. 20). As in Section VIII-B, using the covariance-aware attractor point calculation from (60) and (61) is again crucial. The robot end effector can thus be moved in the plane while always pointing the gripper towards the bottle. The precision matrix at the robot configuration of Fig. 20 evaluates to

$$P = \begin{bmatrix} 9 & 10 & 7 & -12 & 13 & 32 \\ 10 & 760 & -17 & 80 & 18 & 49 \\ 7 & -17 & 990 & -8 & 28 & * \\ -12 & 80 & -8 & 720 & 96 & -2 \\ 13 & 18 & 28 & 96 & 340 & 37 \\ 32 & 49 & * & -2 & 37 & 830 \end{bmatrix}. \quad (46)$$

With  $\lambda_{rot}^- = 100$ ,  $\lambda_{rot}^+ = 500$ ,  $\lambda_{trans}^- = 100$ ,  $\lambda_{trans}^+ = 500$ ,  $k_{trans,nom} = 300$  and  $k_{rot,nom} = 100$ , we obtain the stiffness

$$K = \begin{bmatrix} * & 4.1 & 2.3 & * & * & * \\ 4.1 & 300 & * & 31 & 7.2 & 19 \\ 2.3 & * & 300 & -1.9 & 8.7 & * \\ * & 31 & -1.9 & 99 & 14 & 2.6 \\ * & 7.2 & 8.7 & 14 & 52 & -1.7 \\ * & 19 & * & 2.6 & -1.7 & 100 \end{bmatrix} \quad (47)$$

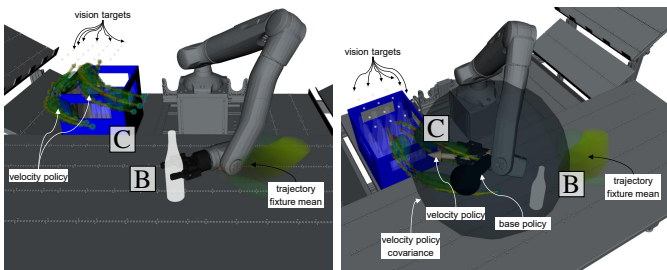


Fig. 20: Picking up a bottle [B] for moving it into a crate [C] using position-based trajectory, velocity and visual servoing fixtures. The rotationally symmetric bottle can be picked up from any angle thanks to a probabilistic trajectory fixture learned from demonstrations on  $\mathcal{M}_2$  with variable stiffness resulting in the stiffness matrix in (47) (left). After [B] has been picked up, the velocity fixture takes over, fusing a *stabilizing policy* with the learned policy (right). This fixture aids the operator to move to [C] where a probabilistic visual servoing fixture allows to select different placement positions.

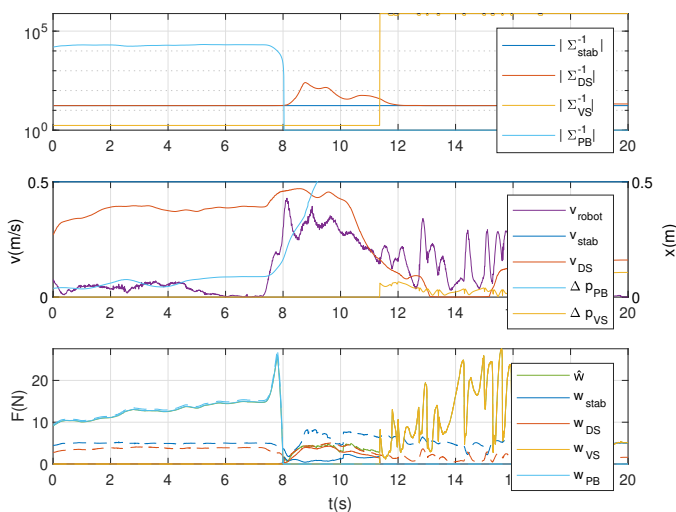


Fig. 21: Norm of covariances (top), target velocities and position offset (middle), raw (dashed,  $w_{VF,i}$ ) and arbitrated (solid lines,  $\hat{\Sigma}_{VF}^{-1} \Sigma_{VF,i}^{-1} w_{VF,i}$  resp.  $\hat{w}$ , see (16)) fixture forces (bottom) of the *stabilizing policy*, DS-based, trajectory and visual servoing fixtures used for manipulating the bottle.

with  $*$  denoting values  $< 1$ . The covariance adaptation using the Mahalanobis distance (Section VI-C) is also crucial. Setting a maximum distance value of 5 for this unitless distance, the fixture remains active for larger displacements around the rotational DoF (up to  $41^\circ$ ) than for other DoFs (up to 7.1 cm) for the given precision. Once the bottle has been picked up, the operator can easily escape this fixture by achieving a displacement larger than this threshold.

After leaving the position-based VF, the DS-based VF takes over. Learned from 5 demonstrations, it is encoded in a KMP based on a GMM with  $M = 5$  Gaussians with hyperparameters  $\lambda = 0.1$ ,  $\lambda_c = 10$ ,  $\alpha = 0.1$ ,  $h = 1$  and  $l = 0.1$  for the position velocity and  $l = 0.03$  for the orientation velocity field. This DS moves the operator towards the visual servoing VF while keeping the bottle upright.

We again simulate visual measurements for all  $M = 20$  crate positions with  $\Sigma = 2.25 \times 10^{-1} \cdot \mathbf{I}_6$ . For the visual servoing fixture, we use a length scale  $l = (0.006, 0.006, 0.2, 0, 0, 0)$  and a deadzone of 5 mm in the  $xy$  plane.

Figure 21 visualizes covariances, target velocities, position

offset as well as raw and arbitrated forces summing to  $\hat{w}$  (16) of the exemplary execution from the supplementary video.

To integrate user feedback for our approach<sup>4</sup>, we have asked six expert users (2 female, 4 male) aged 27-42 ( $M = 35.2$ ,  $SD = 5.6$ ) who regularly work with shared control methods and haptic interfaces but were not involved with this work to perform the task of picking the bottle and placing it in a predefined position in the crate using our fixtures. After familiarization with the system, each user performs the task 4 times, with either no obstacle, an obstacle close to the picking position or on the way to the crate, or both obstacles. We systematically vary the order of those 4 trials in a latin square design. Over all 24 trials, users succeeded in placing the bottle with a success rate of 87.5%. The failure situation was always that users dropped the bottle slightly out of place so that it would tip over instead of landing in the holder position. After the experiment, we asked users to rate the system using both the NASA TLX [63] ( $M : 4.7$ ,  $SD : 1.4$ , range: 1 – 20, lower = better) as well as the SUS [64] ( $M : 89$ ,  $SD : 6.6$ , range: 0 – 100, higher = better) questionnaires. Both values hint at a high usability of the system requiring low effort from the operator.

We have complemented this initial heuristic evaluation by a *semi-structured interview* about the type of guidance expected by users for this task, its implementation with this method – also regarding the forces experienced – and finally also about transitions between different phases of the task. The users in general reported a close to optimal guidance with no notable transitions, however highlighting that forces when placing the bottle were too high. This is also reflected in the physical demand of the TLX score ( $M : 7.2$ ,  $SD : 3.9$ ) being higher than the average TLX score. We furthermore asked users to rate the forces on a scale from 0 (forces too low) to 10 (forces too high), which is with  $M : 6.7$ ,  $SD : 1.1$  slightly leaning towards too high forces. This shortcoming can easily be corrected by lowering the stiffness of the visual servoing VF, as confirmed by the subjects via an additional trial after completion of the experiment.

## IX. DISCUSSION

### A. Dynamical-Systems-based Virtual Fixtures

VFs based on DSs as evaluated also in combination with other fixtures in Sections VIII-C and VIII-E to VIII-G allow for a collaborative automation. By default, the task is being performed autonomously while human interaction is always possible as can be seen in the supplementary video.

A major challenging problem in DS-based VFs is the need to find the right hyperparameters both for the learned as well as for the *stabilizing policy*. When using a GP for modeling the DS, it is especially important to ensure that its covariance output fits the other fixtures present, i.e. it should not output a too low covariance when another, better suited fixture can take over. On the other hand, its uncertainty should also not be too high as it would not take any effect otherwise. This modeling is greatly simplified through the use of KMP-based policies,

<sup>4</sup>Ethical approval obtained from the ‘‘Geschäftsstelle Forschungsethik’’ of the German Aerospace Center (DLR) under number 15/24.

where the underlying GMM already models the covariance appropriately. This leaves the covariance tuning to the *stabilizing policy*, which is equipped with a constant covariance through (31). Future work should consider approaches to automatically select viable hyperparameters in the fixture’s kernel as well as for this constant covariance value from demonstrations.

A limitation of the current formulation is that only a global, but no per-DoF epistemic uncertainty estimate of the velocity policy is available through the kernels (27). This was alleviated by using different policies for positional and orientational control; however, as for the coupled stiffness (Section IV-B), a policy unifying all DoFs would be desirable. Such policy could then, through the arbitration (16), progress some DoFs through the DS evolution while the remaining DoFs would be brought back to the demonstration data by the *stabilizing policy*. Such behavior is especially relevant in VFs, as perturbations induced by the operator are a desired property of the overall system.

### B. Probabilistic Policy Arbitration via Products of Experts

Previous works have already shown that a probabilistic arbitration scheme allows for an optimal combination of different VFs [8]. Throughout the evaluation, we have seen how this arbitration naturally extends to other types of VFs and manifolds and is essential for combining learned and *stabilizing* policies. One can thus always choose the best VF representation for a specific task phase without manually designing transitions, highlighting the advantages of our fully probabilistic VF formulation. One key distinction to previous works is that our formulation supports different manifolds  $\mathcal{M}$  by transforming the wrench to a common representation in the cotangent space of  $\mathbb{R}^3 \times S^3$ . Fusing the different fixtures in wrench space, naturally, different types of VFs are supported. This allows to easily fuse fixtures calculating an attractor point, a target velocity or directly a wrench in a unified formulation which in turn allows to model guiding behavior for each portion of a task using the best available fixture representation.

### C. Variable Stiffness

Previous works [8], [41] either considered diagonal or block-diagonal stiffness matrices. While such formulations are well suited when high covariance only appears within positions or orientations, block-diagonal stiffness matrices fail when a lower stiffness is required along a coupled DoF as in Section VIII-A. Clearly, such coupled variable stiffness is only possible with our method. In this experiment, our approach achieves to model a stiffness that makes the robot’s end effector follow the geodesic between two detections. Our approach furthermore provides reasonable stiffness values for the precision matrices observed in all experiments. This underlines that the proposed approach is suitable for the generation of stiffness matrices from arbitrary precision matrices.

## X. CONCLUSION

In this work we introduce a unified, probabilistic Virtual Fixture framework providing different types of assistance to

operators – particularly **coarse**, **precise** and **very precise** guidance – where each type of fixture can either be manually defined or learned from human demonstrations. To address a gap in the literature – namely, the limited attention given to learned virtual fixtures that actively support task progression – we propose a novel, uncertainty-aware Dynamical System-based Virtual Fixture formulation enabling flexible task automation while keeping the operator in control. We further introduce geometry-awareness in shared control through object-specific coordinate systems, including Cartesian, cylindrical and spherical frames. Combined with a novel variable impedance formulation – which robustly captures correlations between DoFs – our framework brings together the different fixture types using a *product of experts* approach, enabling a principled and uncertainty-aware fusion of assistance commands.

We have validated that the approach can be readily applied across diverse use cases, thanks to its ease of programming and flexibility with respect to fixture representations, input modalities, and uncertainty sources. The evaluation with 6 expert users hints at a high usability of our method, paired with low workload for human operators. While we demonstrated its use in factory automation and space scenarios and in an initial experiment with expert users, we believe that the approach is also well-suited for medical and personal assistance robotics, which we plan to investigate in future work. In this regard, a full user study should be conducted to precisely validate the effectiveness of our approach. We furthermore envision developing methods to interactively modify position-based fixtures, allowing an operator to modify them adaptively based on novel task needs [65]. To ease finding working hyperparameters for the geometric visual servoing fixture, methods for automatic tuning should be investigated. Finally, to enable the use of the proposed framework in high-latency applications such as on-orbit servicing, we plan to integrate it with controllers that can provide stable force feedback despite such delays.

## REFERENCES

- [1] L. Rosenberg, “Virtual fixtures: Perceptual tools for telerobotic manipulation,” in *Proceedings of IEEE Virtual Reality Annual International Symposium*, 1993, pp. 76–82.
- [2] S. A. Bowyer, B. L. Davies, and F. R. y Baena, “Active constraints/virtual fixtures: A survey,” *IEEE Transactions on Robotics*, vol. 30, no. 1, pp. 138–157, Feb 2014.
- [3] K. Haggmann, A. Hellings-Kuss, F. Steidle, F. Stulp, D. Leidner, and J. Klodmann, “Continuous transitions between levels of autonomy based on virtual fixtures for surgical robotic systems,” in *2024 IEEE/RSJ International Conference on Intelligent Robots and Systems, IROS 2024 (submitted)*, 2024. [Online]. Available: <https://elib.dlr.de/203851/>
- [4] A. Wicht, T. Franke, A. Hahn, N. Håkansson, C. Kürbis, R. Smol, T. Hulin, T. Eiband, P. Lehner, M. Mühlbauer, K. Nottensteiner, R. Pietschmann, B. Thaler, D. Thaler, and J. Bosse, “Human-centric concept for a reconfigurable robotic system enabling low-volume assembly of photonic and quantum modules,” in *2025 IEEE/SICE International Symposium on System Integration (SII)*. IEEE, 01 2025, pp. 1241–1246.
- [5] F. Leutert, D. Bohlig, F. Kempf, K. Schilling, M. Mühlbauer, B. Ayan, T. Hulin, F. Stulp, A. Albu-Schäffer, V. Kutscher, C. Plesker, T. Dasbach, S. Damm, R. Anderl, and B. Schleich, “Ai-enabled cyber–physical in-orbit factory - ai approaches based on digital twin technology for robotic small satellite production,” *Acta Astronautica*, vol. 217, pp. 1–17, 04 2024.
- [6] M. Mühlbauer, F. Leutert, C. Plesker, L. X. Wiedmann, A. M. Giordano, J. Silverio, T. Hulin, F. Stulp, J. Voges, R. Knobloch, K. Schilling, B. Schleich, and A. O. Albu-Schäffer, “Ai-based robust and failure-tolerant processes for in-orbit manufacturing of modular small satellites,” in *75th International Astronautical Congress, IAC 2024*, 10 2024.

- [7] M. Mühlbauer, F. Steinmetz, F. Stulp, T. Hulin, and A. Albu-Schäffer, "Multi-phase multi-modal haptic teleoperation," in *2022 IEEE/RSJ International Conference on Intelligent Robots and Systems (IROS)*. IEEE, 10 2022.
- [8] M. Mühlbauer, T. Hulin, B. Weber, S. Calinon, F. Stulp, A. Albu-Schäffer, and J. Silvério, "A probabilistic approach to multi-modal adaptive virtual fixtures," *IEEE Robotics and Automation Letters*, vol. 9, no. 6, pp. 5298–5305, 2024.
- [9] A. Birk, G. Antonelli, P. Di Lillo, E. Simetti, G. Casalino, G. Indiveri, L. Ostuni, A. Turetta, A. Caffaz, P. Weiss, T. Gobert, T. Doernbach, B. Chemisky, J. Gancet, T. Siedel, S. Govindaraj, X. Martinez, P. Letier, C. Mueller, T. Luczynski, A. Gomez Chavez, D. Koehntopp, A. Kupcsik, S. Calinon, and A. K. Tanwani, "Dexterous underwater manipulation from onshore locations: Streamlining efficiencies for remotely operated underwater vehicles," *IEEE Robotics & Automation Magazine*, vol. 25, no. 4, pp. 24–33, 12 2018.
- [10] A. Ijspeert, J. Nakanishi, and S. Schaal, "Movement imitation with nonlinear dynamical systems in humanoid robots," in *2002 IEEE International Conference on Robotics and Automation*. IEEE, 05 2002, pp. 1398–1403.
- [11] A. J. Ijspeert, J. Nakanishi, H. Hoffmann, P. Pastor, and S. Schaal, "Dynamical movement primitives: Learning attractor models for motor behaviors," *Neural Computation*, vol. 25, no. 2, pp. 328–373, 2013.
- [12] M. Saveriano, F. J. Abu-Dakka, A. Kramberger, and L. Peternel, "Dynamic movement primitives in robotics: A tutorial survey," *The International Journal of Robotics Research*, vol. 42, no. 13, pp. 1133–1184, 2023.
- [13] P. C. Lopez-Custodio, K. Bharath, A. Kucukyilmaz, and S. Preston, "Non-parametric regression for robot learning on manifolds," *arXiv preprint arXiv:2310.19561*, 2023.
- [14] B. Fichera, S. Borovitskiy, A. Krause, and A. G. Billard, "Implicit manifold gaussian process regression," in *Advances in Neural Information Processing Systems*, A. Oh, T. Naumann, A. Globerson, K. Saenko, M. Hardt, and S. Levine, Eds., vol. 36. Curran Associates, Inc., 2023, pp. 67 701–67 720.
- [15] S. M. Khansari-Zadeh and A. Billard, "Learning stable nonlinear dynamical systems with gaussian mixture models," *IEEE Transactions on Robotics*, vol. 27, no. 5, pp. 943–957, 2011.
- [16] B. Fichera and A. Billard, "Linearization and identification of multiple-attractor dynamical systems through laplacian eigenmaps," *J. Mach. Learn. Res.*, vol. 23, no. 1, Jan 2022.
- [17] —, "Learning dynamical systems encoding non-linearity within space curvature," 2024. [Online]. Available: <https://arxiv.org/abs/2403.11948>
- [18] H. B. Mohammadi, S. Hauberg, G. Arvanitidis, N. Figueroa, G. Neumann, and L. Rozo, "Neural contractive dynamical systems," in *The Twelfth International Conference on Learning Representations*, 2023.
- [19] R. Pérez-Dattari, C. Della Santina, and J. Kober, "Puma: Deep metric imitation learning for stable motion primitives," *Advanced Intelligent Systems*, vol. 6, no. 11, 2024.
- [20] R. Pérez-Dattari and J. Kober, "Stable motion primitives via imitation and contrastive learning," *IEEE Transactions on Robotics*, vol. 39, no. 5, pp. 3909–3928, 2023.
- [21] G. Raiola, S. S. Restrepo, P. Chevalier, P. Rodriguez-Ayerbe, X. Lamy, S. Tliba, and F. Stulp, "Co-manipulation with a library of virtual guiding fixtures," *Autonomous Robots*, vol. 42, no. 5, pp. 1037–1051, Nov 2017.
- [22] B. Ti, A. Razmjoo, Y. Gao, J. Zhao, and S. Calinon, "A geometric optimal control approach for imitation and generalization of manipulation skills," *Robotics and Autonomous Systems*, vol. 164, p. 104413, 2023.
- [23] G. Franzese, A. Meszaros, L. Peternel, and J. Kober, "Ilosa: Interactive learning of stiffness and attractors," in *2021 IEEE/RSJ International Conference on Intelligent Robots and Systems (IROS)*. IEEE, 09 2021, pp. 7778–7785.
- [24] A. Meszaros, G. Franzese, and J. Kober, "Learning to pick at non-zero-velocity from interactive demonstrations," *IEEE Robotics and Automation Letters*, vol. 7, no. 3, pp. 6052–6059, 2022.
- [25] E. Pignat and S. Calinon, "Bayesian gaussian mixture model for robotic policy imitation," *IEEE Robotics and Automation Letters*, vol. 4, no. 4, pp. 4452–4458, 2019.
- [26] D. Papageorgiou, F. Dimeas, T. Kastritsi, and Z. Doulgeri, "Kinesthetic guidance utilizing dmp synchronization and assistive virtual fixtures for progressive automation," *Robotica*, vol. 38, no. 10, pp. 1824–1841, 2019.
- [27] A. Pervez, H. Latifee, J.-H. Ryu, and D. Lee, "Motion encoding with asynchronous trajectories of repetitive teleoperation tasks and its extension to human-agent shared teleoperation," *Autonomous Robots*, vol. 43, no. 8, pp. 2055–2069, 2019.
- [28] X. Chen, Y. Michel, and D. Lee, "Closed-loop variable stiffness control of dynamical systems," in *2020 IEEE-RAS 20th International Conference on Humanoid Robots (Humanoids)*. IEEE, 07 2021.
- [29] H. Xue, Y. Michel, and D. Lee, "A shared control approach based on first-order dynamical systems and closed-loop variable stiffness control," *Journal of Intelligent & Robotic Systems*, vol. 109, no. 4, 2023.
- [30] W. Amanhoud, M. Khoramshahi, and A. Billard, "A dynamical system approach to motion and force generation in contact tasks," in *Proceedings of Robotics: Science and Systems*, June 2019.
- [31] K. Hagemann, A. Hellings-Kuß, J. Klodmann, R. Richter, F. Stulp, and D. Leidner, "A digital twin approach for contextual assistance for surgeons during surgical robotics training," *Frontiers in Robotics and AI*, vol. 8, 2021.
- [32] V. Pruks and J.-H. Ryu, "Method for generating real-time interactive virtual fixture for shared teleoperation in unknown environments," *The International Journal of Robotics Research*, vol. 41, no. 9–10, pp. 925–951, 2022.
- [33] A. Bettini, P. Marayong, S. Lang, A. Okamura, and G. Hager, "Vision-assisted control for manipulation using virtual fixtures," *IEEE Transactions on Robotics*, vol. 20, no. 6, pp. 953–966, 2004.
- [34] M. J. A. Zeestraten, I. Havoutis, and S. Calinon, "Programming by demonstration for shared control with an application in teleoperation," *IEEE Robotics and Automation Letters*, vol. 3, no. 3, pp. 1848–1855, 2018.
- [35] J. J. Abbott, P. Marayong, and A. M. Okamura, "Haptic virtual fixtures for robot-assisted manipulation," in *Robotics Research: Results of the 12th International Symposium ISRR*. Springer, 2007, pp. 49–64.
- [36] Z. Pezzementi, A. M. Okamura, and G. D. Hager, "Dynamic guidance with pseudo-admittance virtual fixtures," in *Proceedings 2007 IEEE International Conference on Robotics and Automation*, 2007, pp. 1761–1767.
- [37] N. Hogan, "Impedance control: An approach to manipulation," in *1984 American Control Conference*. IEEE, 07 1984.
- [38] Y. Michel, R. Rahal, C. Pacchierotti, P. R. Giordano, and D. Lee, "Bilateral teleoperation with adaptive impedance control for contact tasks," *IEEE Robotics and Automation Letters*, vol. 6, no. 3, pp. 5429–5436, 2021.
- [39] Y. Michel, M. Saveriano, F. J. Abu-Dakka, and D. Lee, "Orientation control with variable stiffness dynamical systems," in *2023 IEEE/RSJ International Conference on Intelligent Robots and Systems (IROS)*. IEEE, 10 2023.
- [40] R. Balachandran, M. De Stefano, H. Mishra, C. Ott, and A. Albu-Schaeffer, "Passive arbitration in adaptive shared control of robots with variable force and stiffness scaling," *Mechatronics*, vol. 90, p. 102930, 2023.
- [41] F. Abi-Farraj, T. Osa, N. P. J. Peters, G. Neumann, and P. R. Giordano, "A learning-based shared control architecture for interactive task execution," in *2017 IEEE International Conference on Robotics and Automation (ICRA)*. IEEE, 05 2017.
- [42] S. Huang and J. M. Schimmels, "Achieving an Arbitrary Spatial Stiffness with Springs Connected in Parallel," *Journal of Mechanical Design*, vol. 120, no. 4, pp. 520–526, 12 1998.
- [43] S. Huang and J. Schimmels, "The eigenscrew decomposition of spatial stiffness matrices," *IEEE Transactions on Robotics and Automation*, vol. 16, no. 2, pp. 146–156, 2000.
- [44] M. Selvaggio, M. Cognetti, S. Nikolaidis, S. Ivaldi, and B. Siciliano, "Autonomy in physical human-robot interaction: A brief survey," *IEEE Robotics and Automation Letters*, vol. 6, no. 4, pp. 7989–7996, 2021.
- [45] M. Selvaggio, G. Notomista, F. Chen, B. Gao, F. Trapani, and D. Caldwell, "Enhancing bilateral teleoperation using camera-based online virtual fixtures generation," in *2016 IEEE/RSJ International Conference on Intelligent Robots and Systems (IROS)*. IEEE, 10 2016.
- [46] F. Abi-Farraj, C. Pacchierotti, O. Arenz, G. Neumann, and P. R. Giordano, "A haptic shared-control architecture for guided multi-target robotic grasping," *IEEE Transactions on Haptics*, vol. 13, no. 2, pp. 270–285, 2020.
- [47] M. J. A. Zeestraten, I. Havoutis, J. Silvério, S. Calinon, and D. G. Caldwell, "An approach for imitation learning on Riemannian manifolds," *IEEE Robotics and Automation Letters*, vol. 2, no. 3, pp. 1240–1247, 2017.
- [48] S. Calinon, "Gaussians on riemannian manifolds: Applications for robot learning and adaptive control," *IEEE Robotics & Automation Magazine*, vol. 27, no. 2, pp. 33–45, 2020.
- [49] J. M. Lee, *Introduction to Smooth Manifolds*. Springer New York, 2003.
- [50] S. Calinon, "A tutorial on task-parameterized movement learning and retrieval," *Intelligent Service Robotics*, vol. 9, no. 1, pp. 1–29, Sep 2015.

- [51] R. A. Jacobs, M. I. Jordan, S. J. Nowlan, and G. E. Hinton, "Adaptive mixtures of local experts," *Neural Computation*, vol. 3, no. 1, pp. 79–87, 1991.
- [52] C. K. Williams and C. E. Rasmussen, *Gaussian processes for machine learning*. MIT press Cambridge, MA, 2006, vol. 2, no. 3.
- [53] Y. Huang, L. Rozo, J. Silvério, and D. G. Caldwell, "Kernelized movement primitives," *The International Journal of Robotics Research*, vol. 38, no. 7, pp. 833–852, 2019.
- [54] N. Jaquier, V. Borovitskiy, A. Smolensky, A. Terenin, T. Asfour, and L. Rozo, "Geometry-aware bayesian optimization in robotics using riemannian matérn kernels," in *Proceedings of the 5th Conference on Robot Learning*, ser. Proceedings of Machine Learning Research, A. Faust, D. Hsu, and G. Neumann, Eds., vol. 164. PMLR, 08–11 Nov 2022, pp. 794–805.
- [55] G. Hinton, "Products of experts," in *9th International Conference on Artificial Neural Networks: ICANN '99*, vol. 1999. IEEE, 1999, pp. 1–6.
- [56] M. Dyck, A. Sachtler, J. Klodmann, and A. Albu-Schaffer, "Impedance control on arbitrary surfaces for ultrasound scanning using discrete differential geometry," *IEEE Robotics and Automation Letters*, vol. 7, no. 3, pp. 7738–7746, 2022.
- [57] G. Chen, H. Wang, Z. Lin, and X. Lai, "The principal axes decomposition of spatial stiffness matrices," *IEEE Transactions on Robotics*, vol. 31, no. 1, pp. 191–207, 2015.
- [58] S. Huang and J. M. Schimmels, "Comments on "the principal axes decomposition of spatial stiffness matrices"," *IEEE Transactions on Robotics*, vol. 31, no. 6, pp. 1561–1564, 2015.
- [59] S. Calinon and D. Lee, "Learning control," in *Humanoid robotics: A reference*. Springer Netherlands, 2017, pp. 1–52.
- [60] S. Salvador and P. Chan, "Toward accurate dynamic time warping in linear time and space," *Intelligent Data Analysis*, vol. 11, no. 5, pp. 561–580, 2007.
- [61] C. M. Bishop, *Pattern Recognition and Machine Learning*, ser. Information Science and Statistics. Springer, 2006.
- [62] M. S. Mühlbauer, F. Stulp, A. O. Albu-Schäffer, and J. Silvério, "Mixture of experts on riemannian manifolds for visual-servoing fixtures," in *2022 IEEE/RSJ International Conference on Intelligent Robots and Systems, Workshop on Probabilistic Robotics in the Age of Deep Learning*, Oktober 2022. [Online]. Available: <https://elib.dlr.de/189970/>
- [63] S. G. Hart and L. E. Staveland, "Development of nasa-tlx (task load index): Results of empirical and theoretical research," in *Advances in psychology*. Elsevier, 1988, vol. 52, pp. 139–183.
- [64] J. Brooke *et al.*, "Sus-a quick and dirty usability scale," *Usability evaluation in industry*, vol. 189, no. 194, pp. 4–7, 1996.
- [65] G. Quere, F. Stulp, D. Filliat, and J. Silvério, "A probabilistic approach for learning and adapting shared control skills with the human in the loop," in *2024 IEEE International Conference on Robotics and Automation (ICRA)*. IEEE, 05 2024, pp. 15728–15734.
- [66] A. Albu-Schäffer, C. Ott, U. Frese, and G. Hirzinger, "Cartesian impedance control of redundant robots: recent results with the dlr-light-weight-arms," in *2003 IEEE International Conference on Robotics and Automation*, vol. 3, 2003, pp. 3704–3709 vol.3.

## APPENDIX

### A. Key Notations

Table III summarizes the key notations of our framework.

### B. Variable Impedance Control on $\mathcal{M}_2$ and $\mathcal{M}_3$

The variable impedance formulation of Section IV-B can also be extended to  $\mathcal{M}_2$  and  $\mathcal{M}_3$  introduced in Section III-A. For this, we scale the nominal translational stiffness  $k_{\text{nom},j}$  by the radius  $r$  for the angular DoFs ( $\mathcal{M}_2: j = 1, \mathcal{M}_3: j = 1, 2$ ):

$$k_{\text{nom},j}^* = r \cdot k_{\text{nom},j}. \quad (48)$$

This ensures a stiffness comparable to the Euclidean case for those DoFs, avoiding too high stiffness values for  $r \ll 1$ . As the calculation of the stiffness values is performed in a coordinate system rotated by  $\mathbf{R}_{\text{diag}}^T$ , the maximum translational stiffness values for each DoF in those coordinates has to be limited further s.t. when rotating the stiffness matrix

TABLE III: KEY NOTATIONS USED IN OUR FRAMEWORK.

$N \in \mathbb{N}$	$\triangleq$	Number of data points per demonstration
$N_{\text{DS}}, N_{\text{PB}}, N_{\text{VS}}$	$\triangleq$	Number of fixtures of each type
$M$	$\triangleq$	Number of Gaussian components in a fixture
$\mathbf{x}_{\text{VF},i}$	$\triangleq$	Attractor of the $i$ -th fixture
$\mathbf{w}_{\text{VF},i}$	$\triangleq$	Wrench of the $i$ -th fixture
$\Sigma_{\text{VF},i}$	$\triangleq$	Covariance of the $i$ -th fixture
$\mathbf{K}_{\text{VF},i}$	$\triangleq$	Stiffness matrix of the $i$ -th fixture
$\mathbf{D}_{\text{VF},i}$	$\triangleq$	Damping matrix of the $i$ -th fixture
$\mathbf{k}_{\text{nom}}$	$\triangleq$	Diagonal nominal stiffness values
$\lambda_{\text{trans}}^-, \lambda_{\text{trans}}^+$	$\triangleq$	"High" and "low" translational stiffness eigenvalues
$\lambda_{\text{rot}}^-, \lambda_{\text{rot}}^+$	$\triangleq$	"High" and "low" rotational stiffness eigenvalues
$\lambda, \lambda_c, \alpha$	$\triangleq$	KMP regularization and scaling factors
$l$	$\triangleq$	Length scale for the RBF kernel
$\dot{x}_{\text{stab}}, \sigma_{\text{stab}}$	$\triangleq$	Stabilizing policy velocity and covariance
$d_{\text{min}}, d_{\text{max}}$	$\triangleq$	Start and end of distance-based covariance adaptation
$L$	$\triangleq$	Length scale of the visual servoing fixture
$\gamma$	$\triangleq$	Regularization factor
$L_{\text{dead}}, r_{\text{dead}}$	$\triangleq$	Length scale and radius of the deadzone
$L_{\text{add}}, L_{\text{dead,add}}, r_{\text{dead,add}}$	$\triangleq$	Length scale and deadzone parameters of the additional expert

back, the nominal stiffness value is not exceeded. This can be achieved by limiting the maximum value of the stiffness  $\mathbf{k}_{\text{nom,trans}}$  denoting the translational ( $j = 1, 2, 3$ ) DoFs of  $\mathbf{k}_{\text{nom}}$  in rotated DoFs through

$$\mathbf{k}_{\text{rot}} = \text{diag}(\mathbf{R}_{\text{diag}}^T \text{diag}(\mathbf{k}_{\text{nom,trans}}) \mathbf{R}_{\text{diag}}) \quad (49)$$

$$\mathbf{k}_{\text{rotback}} = \text{diag}(\mathbf{R}_{\text{diag}} \text{diag}(\mathbf{k}_{\text{rot}}) \mathbf{R}_{\text{diag}}^T) \quad (50)$$

$$\beta = \max(\mathbf{k}_{\text{rotback}} \oslash \mathbf{k}_{\text{nom,trans}}) \quad (51)$$

$$\mathbf{k}'_{\text{nom,trans}} = \beta \mathbf{k}_{\text{rot}} \quad (52)$$

where  $\text{diag}$  transforms a vector to a diagonal matrix respectively extracts the diagonal of a matrix and  $\oslash$  is the element wise vector division. In (49), we take the diagonal elements of  $\mathbf{k}_{\text{nom,trans}}$  rotated into coordinates of  $\mathbf{P}'_{\text{VF},i}$ . As the maximum values of the translational stiffnesses correspond to  $\text{diag}(\mathbf{k}_{\text{rot}})$ , we can rotate that matrix back and check for potentially increased stiffness values in (51). The maximum value of this increase is then used to scale the translational stiffnesses.

### C. Optimal Damping using Double Diagonalization

We design the damping matrix  $\mathbf{D}_i$  using double diagonalization as presented in [66] with  $\zeta = 0.7$ , in particular

$$\mathbf{D}_i = 2\zeta \mathbf{Q} \mathbf{K}_{i,0}^{\frac{1}{2}} \mathbf{Q}^T \quad (53)$$

with mass matrix  $\mathbf{M}_{i,\mathcal{M}} = \mathbf{Q} \mathbf{Q}^T$  and stiffness matrix  $\mathbf{K}_i^* = \mathbf{Q} \mathbf{K}_{i,0} \mathbf{Q}^T$  where  $\mathbf{K}_{i,0}$  is a diagonal matrix. Similar to the wrench transformation in the previous section, a Cartesian mass matrix  $\mathbf{M}_{\text{cart}}$  has to be transformed to the manifold using

$$\mathbf{M}_{i,\mathcal{M}} = (\mathbf{J}_{i,\mathcal{M}} \mathbf{M}_{\text{cart}}^{-1} \mathbf{J}_{i,\mathcal{M}}^T)^{-1}. \quad (54)$$

To also dampen zero-stiffness DoFs, we calculate  $\mathbf{K}_i^*$  with scaling factors  $s_j$  used in (21) and (23) lower-bounded to a small  $\epsilon > 0$ , thus ensuring smoothly decaying robot motions.

#### D. Teleoperation System

To supply the operator with force feedback, we use the bilateral teleoperation system of [7], [8]. We assume that the haptic input device can also be controlled using Cartesian wrenches; in case of a torque-controlled robot, (3) can be used to compute joint torques. Using a simple position-computed force architecture that does not require a force-torque sensor at the end effector, the Cartesian wrenches of remote robot  $w_{ee,rem}$  and input device  $w_{ee,inp}$  are

$$w_{ee,rem} = \chi \left( K \text{Log}_{x_{ee}}^M(x_{inp}) + D \frac{d}{dt} \text{Log}_{x_{ee}}^M(x_{inp}) \right) + w_{VF} \quad (55)$$

$$w_{ee,inp} = -\chi \text{Ad}_{ir} w_{ee,remote}. \quad (56)$$

The user receives force feedback from both the environment as well as the VFs through the coupling introduced by  $\chi$ , the adjoint  $\text{Ad}_{ir}$  transforms wrenches between coordinate systems of the remote robot and the input device. By applying the VF wrench to the robot performing the task, we can support a user while avoiding potential inaccuracies resulting from a teleoperated coupling.

#### E. KMP with Covariance in Pose Space for DS

First, we approximate the joint distribution between  $x$  and  $\dot{x}$  in a GMM with  $M$  components and use GMR to compute the probabilistic reference velocities  $\mathcal{N}(\dot{x}_{DS} | \mu_{GMR}, \Sigma_{GMR})$ . Through the averaging of the GMM, this results in a smooth velocity field. As the wrench calculated from this DS is later fused with wrenches from other VFs, we only use the velocity  $\mu_{GMR}$  resulting from the mixture regression. The covariance output  $\Sigma_{GMR}$  of the regression is discarded, as it would correspond to a covariance in velocity space which is not well suited for the fusion with fixtures with covariance in pose space. To obtain a better suiting covariance in pose space, we decompose data points  $\xi_j$  and the  $M$  Gaussians of the GMM

$$\xi_j = \begin{bmatrix} x_j \\ \dot{x}_j \end{bmatrix}, \quad \mu_m = \begin{bmatrix} \mu_m^I \\ \mu_m^O \end{bmatrix}, \quad \Sigma_m = \begin{bmatrix} \Sigma_m^I & \Sigma_m^{IO} \\ \Sigma_m^{OI} & \Sigma_m^O \end{bmatrix} \quad (57)$$

which in turn allows to write a marginalized GMM using the weight factors  $\pi_m$  from the joint encoding (5)

$$p_n(x) = \sum_{m=1}^M \pi_m \mathcal{N}(x | \mu_m^I, \Sigma_m^I) \quad (58)$$

and to compute the likelihood of each Gaussian generating  $x$

$$e_m = \frac{\pi_m \mathcal{N}(x | \mu_m^I, \Sigma_m^I)}{\sum_{m=1}^M \pi_m \mathcal{N}(x | \mu_m^I, \Sigma_m^I)}. \quad (59)$$

Using those weighting factors, we compute  $\hat{\Sigma}$  through a unimodal approximation (7) of the GMM (58). This results in a probabilistic velocity field  $\mathcal{N}(\mu_{GMR}, \hat{\Sigma})$ . We sample this velocity field at a subsampled set of  $N_{ref}$  poses from the demonstrated trajectories to obtain a probabilistic reference  $\{\mu_{GMR,n}, \hat{\Sigma}_n\}_{n=1}^{N_{ref}}$  which is then encoded into the KMP. Finally, KMP mean and covariance predictions (8), (9) provide  $\mu_{DS}$ ,  $\Sigma_{DS}$  in (26) at each end effector pose  $x_{ee}$ .

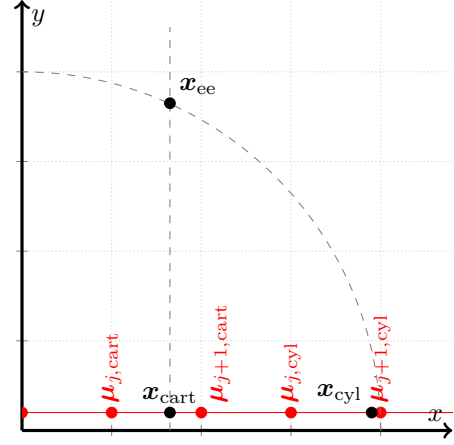


Fig. 22: 2D projection of  $x_{ee}$  and the closest poses  $\mu_j$  and  $\mu_{j+1}$  on a trajectory (red points) in  $\mathcal{M}_1(x_{cart})$  as well as  $\mathcal{M}_{23}(x_{cyl})$ . The  $x$  axis through  $x_{ee}$  as well as the circle with the same radius on  $S^1 \times \mathbb{R}^2 \times S^3$  is plotted in dashed gray, note that according to the manifold metric the closest pose is much further to the right than for Cartesian coordinates.

#### F. On-Manifold Covariance-aware Interpolation

In the real-time controller, the two closest poses  $\mu_j$  and  $\mu_{j+1}$  of this trajectory according to the on-manifold Mahalanobis distance  $d_{\Sigma_j^M}^M(\mu_n, x_{ee})$  (2) are extracted. To guarantee constant runtime, we first extract the 10 closest poses in a background thread while the actual real time computations only use those 10 closest poses. For simplicity we use only the position part of the pose in the distance function, where we set the last three entries of  $\mu_j$  and  $x_{ee}$ , which correspond to the orientation, to the identity. We found only using the position to be sufficient in manipulation scenarios. Adding the orientation to the distance function could help in scenarios where parts of the trajectory pass very close to each other, at the cost of having to tune a scaling factor between position and orientation. We then perform linear interpolation between both extracted closest poses along the covariance-deformed geodesic on the manifold (Fig. 22), using

$$\begin{aligned} \Delta \mu_{j,j+1} &= \text{Log}_{\mu_j}^M \mu_{j+1}, & \Delta \mu_{j,ee} &= \text{Log}_{\mu_j}^M x_{ee}, & (60) \\ \nu &= \frac{\Delta \mu_{j,ee}^\top \Sigma_j^{-1} \Delta \mu_{j,j+1}}{\Delta \mu_{j,j+1}^\top \Sigma_j^{-1} \Delta \mu_{j,j+1}}, & x_{PB} &= \text{Exp}_{\mu_j}^M(\nu \cdot \Delta \mu_{j,j+1}) & (61) \end{aligned}$$

where  $\Delta \mu_{j,j+1}$  is the vector between  $\mu_j$  and  $\mu_{j+1}$  and  $\Delta \mu_{j,ee}$  between  $\mu_j$  and  $x_{ee}$  in tangent space and  $\Sigma_j^{-1}$  the precision matrix corresponding to  $\mu_j$ . The interpolation factor  $0 \leq \nu \leq 1$  represents the closeness of  $x_{ee}$  to  $\mu_j$  and  $\mu_{j+1}$  and  $x_{VF}$  the final VF pose which is used in (4) to calculate the wrench  $w_{VF,i}$  associated to the fixture. Its computation through (61) takes the Mahalanobis distance between the end effector and the two closest means into account. As we assume the covariance matrix to only vary slowly between points we set  $\Sigma_{PB} = \Sigma_j$  which is associated with  $\mu_j$ , however, interpolation could be performed similarly on the manifold of symmetric positive definite matrices [48].

The manifold-aware attractor calculation through (60) and (61) ensures that only forces orthogonal to the trajectory are

being applied by the fixture and thus the user is in full control of motion along to the trajectory.

### G. Modified Logarithm Map with Deadzone

We calculate  $\text{Log}'_{\mathbf{x}_{ee}}{}^{\mathcal{M}}(\boldsymbol{\mu}_m)$  from  $\text{Log}_{\mathbf{x}_{ee}}{}^{\mathcal{M}}(\boldsymbol{\mu}_m)$  using the length scale vector  $\mathbf{l}_{\text{dead}}$  and the crop length  $r_{\text{crop}}$  as follows:

$$\mathbf{L}_{\text{dead}} = \text{diag}(\mathbf{l}_{\text{dead}}^{-2}) \quad (62)$$

$$r = \sqrt{d_{\mathbf{L}_{\text{dead}}}^{\mathcal{M}}(\mathbf{x}_{ee}, \boldsymbol{\mu}_m)} \quad (63)$$

$$\mathbf{d} = \frac{\text{Log}_{\mathbf{x}_{ee}}{}^{\mathcal{M}}(\boldsymbol{\mu}_m)}{r} \quad (64)$$

$$r_{\text{crop}} = \min(r, r_{\text{dead}}) \quad (65)$$

$$d'_j = \begin{cases} d_j, & l_{\text{dead},j} > 0 \\ 0, & l_{\text{dead},j} = 0 \end{cases} \quad (66)$$

$$\text{Log}'_{\mathbf{x}_{ee}}{}^{\mathcal{M}}(\boldsymbol{\mu}_m) = \text{Log}_{\mathbf{x}_{ee}}{}^{\mathcal{M}}(\boldsymbol{\mu}_m) - r_{\text{crop}} \cdot \mathbf{d}' \quad (67)$$

(63) uses the on-manifold distance (2), (66) ensures that only directions with length vector  $> 0$  get modified.

### H. Coordinate System Conversions

1) *Conversion between  $\mathcal{S}^1 \times \mathbb{R}^2 \times \mathcal{S}^3$  and  $\mathbb{R}^3 \times \mathcal{S}^3$* : Position quantities can be converted from  $\mathcal{M}_1$  to  $\mathcal{M}_2$  using

$$\theta_c = x/r, \quad \theta_s = y/r, \quad r = \sqrt{x^2 + y^2}, \quad z = z \quad (68)$$

where  $\theta_c$  and  $\theta_s$  denote the angle  $\theta$  around the  $z$  axis as complex number. For small  $r$ , the angle  $\theta$  is not well-defined. The quaternion has to be rotated by  $-\theta$ , specifically

$$\mathbf{q}^{\mathcal{M}_2} = \text{Exp}_{\mathbf{I}}^{\mathcal{S}^3} \begin{bmatrix} 0 \\ 0 \\ -\theta \end{bmatrix} \cdot \mathbf{q}^{\mathcal{M}_1}. \quad (69)$$

The inverse conversion can be performed as follows

$$x = r \cdot \theta_c, \quad y = r \cdot \theta_s, \quad z = z, \quad \mathbf{q}^{\mathcal{M}_1} = \text{Exp}_{\mathbf{I}}^{\mathcal{S}^3} \begin{bmatrix} 0 \\ 0 \\ \theta \end{bmatrix} \cdot \mathbf{q}^{\mathcal{M}_2} \quad (70)$$

with  $\theta = \arctan2(\theta_s, \theta_c)$  where  $\arctan2$  is the modified arcus tangens mapping to the full circle  $[-\pi, \pi]$ .

2) *Conversion between  $\mathcal{S}^2 \times \mathbb{R}^1 \times \mathcal{S}^3$  and  $\mathbb{R}^3 \times \mathcal{S}^3$* : Position quantities can be converted from  $\mathcal{M}_1$  to  $\mathcal{M}_3$  using

$$s_0 = x/r, \quad s_1 = y/r, \quad s_2 = z/r, \quad r = \sqrt{x^2 + y^2 + z^2} \quad (71)$$

For very small  $r$ , values  $s_i$  are not well-defined. The quaternion expressing the orientation has to be rotated by the inverse of the rotation  $\mathbf{q}_{\text{align}}$  aligning  $[0, 0, 1]$  with  $[s_0, s_1, s_2]$ :

$$\mathbf{q}^{\mathcal{M}_3} = \mathbf{q}_{\text{align}}^{-1} \cdot \mathbf{q}^{\mathcal{M}_1}. \quad (72)$$

The inverse conversion can be performed as follows

$$x = r \cdot s_0, \quad y = r \cdot s_1, \quad z = r \cdot s_2, \quad \mathbf{q}^{\mathcal{M}_1} = \mathbf{q}_{\text{align}} \cdot \mathbf{q}^{\mathcal{M}_3}. \quad (73)$$

### I. Manifold Jacobians

The manifold Jacobian  $\mathbf{J}_{\mathcal{M}} = \frac{\partial \mathbf{x}_{ee, i, \mathcal{M}}}{\partial \mathbf{x}_{ee, \mathbb{R}^3 \times \mathcal{S}^3}}$  relating  $\dot{\mathbf{x}}^{\mathcal{M}} = \mathbf{J}_{\mathcal{M}} \dot{\mathbf{x}}^{\mathbb{R}^3 \times \mathcal{S}^3}$  and  $\mathbf{w}^{\mathbb{R}^3 \times \mathcal{S}^3} = \mathbf{J}_{\mathcal{M}}^{\top} \mathbf{w}^{\mathcal{M}}$  is derived as in [56]

$$\mathbf{J}_{\mathcal{M}} = \begin{bmatrix} \mathbf{J}_{px} & \mathbf{0} \\ \mathbf{J}_{\omega x} & \mathbf{J}_{\omega \omega} \end{bmatrix} \quad (74)$$

where  $\mathbf{J}_{px}$  denotes position quantities and  $\mathbf{J}_{\omega x}$  the coupling between position and orientation. Both are given for  $\mathcal{M}_2$  and  $\mathcal{M}_3$  in the following. We furthermore have  $\mathbf{J}_{\omega \omega} = \mathbf{I}$  for  $\mathcal{M}$  as the axes of the orientation always coincide.

1)  *$\mathcal{M}_2$  Jacobian*: Cartesian  $x$  and  $y$  coordinates have an influence on the angular DoF of the manifold and on  $r$ :

$$\mathbf{J}_{px} = \begin{bmatrix} \frac{-y}{x^2+y^2} & \frac{x}{x^2+y^2} & 0 \\ \frac{x}{\sqrt{x^2+y^2}} & \frac{y}{\sqrt{x^2+y^2}} & 0 \\ 0 & 0 & 1 \end{bmatrix}. \quad (75)$$

As the  $y$  axis of the base of the orientation points in direction of increasing  $r$ , a coupling between Cartesian  $x / y$  velocities and rotational velocities of the manifold is given by

$$\mathbf{J}_{\omega x} = \mathbf{R}^{\top} \begin{bmatrix} 0 & 0 & 0 \\ 0 & 0 & 0 \\ \frac{y}{x^2+y^2} & \frac{-x}{x^2+y^2} & 0 \end{bmatrix} \quad (76)$$

where  $\mathbf{R}^{\top}$  denotes the orientation in manifold coordinates.

2)  *$\mathcal{M}_3$  Jacobian*:  $x, y, z$  contribute to angular and  $r$  DoFs

$$\mathbf{J}_{px} = \begin{bmatrix} \frac{1}{r} & 0 & 0 \\ 0 & \frac{1}{r} & 0 \\ 0 & 0 & 1 \end{bmatrix} \cdot \mathbf{R}_{\text{align}}^{\top} \quad (77)$$

where  $\mathbf{R}_{\text{align}}$  is the rotation matrix equivalent to  $\mathbf{q}_{\text{align}}$ . For the couplings, we get

$$\mathbf{J}_{\omega x} = \mathbf{R}^{\top} \cdot \begin{bmatrix} 0 & \frac{1}{r} & 0 \\ -\frac{1}{r} & 0 & 0 \\ 0 & 0 & 0 \end{bmatrix} \cdot \mathbf{R}_{\text{align}}^{\top} \quad (78)$$

where  $\mathbf{R}^{\top}$  again denotes the orientation in manifold coordinates.